Nano Research

Open Access

Review Article

Research progress on composite electrocatalysts for alkaline hydrogen oxidation reaction

Siqi Lu[1,2]✉, Qingqing Lv[3,4], Yanan Chen[3,4], Tianheng Lu[3,4], Wei Zhu[3,4], and Zhongbin Zhuang[3,4]✉

[1] *School of Mining, Chemistry and Chemical Engineering, Hulunbuir University, Hulunbuir 021008, China*
[2] *Engineering Research Center for Safe Exploitation and Comprehensive Utilization of Mineral Resources at Universities of Inner Mongolia Autonomous Region, Hulunbuir 021008, China*
[3] *State Key Laboratory of Organic–Inorganic Composites and Beijing Advanced Innovation Center for Soft Matter Science and Engineering, Beijing University of Chemical Technology, Beijing 100029, China*
[4] *Beijing Key Laboratory of Intelligent Design and Manufacturing for Hydrogen Energy Materials, Beijing University of Chemical Technology, Beijing 100029, China*

Cite this article: *Nano Research*, **2026**, *19*, 94908551. https://doi.org/10.26599/NR.2026.94908551

ABSTRACT: The commercialization of anion exchange membrane fuel cells (AEMFCs) is hindered by the sluggish kinetics of the hydrogen oxidation reaction (HOR) under alkaline conditions, necessitating the development of electrocatalysts with high activity, long-term durability, and reduced noble-metal loading. Current understanding of the reaction mechanism has evolved from the conventional binary adsorption model based on catalyst–intermediate interactions to a more comprehensive dynamic framework involving catalyst–intermediate–interfacial water ternary cooperation. In recent years, composite electrocatalysts have emerged as promising candidates, where strategies, such as interfacial electronic modulation, oxygen-vacancy engineering, hydrogen spillover, and bifunctional-site synergy, have markedly optimized intermediate adsorption behavior and tailored the interfacial water environment. These advances have significantly enhanced alkaline HOR activity and resistance to poisoning. This review classifies composite electrocatalysts by the periodic groups of their constituent elements, covering oxides (Groups IVB–VIIB), non-oxides, such as carbides and nitrides, as well as the emerging single-atom catalysts. Recent progress in rational design, mechanistic insights, and performance optimization is summarized, with particular emphasis on the relationship between electronic/interfacial structure and catalytic activity. Building on these advances, the key challenges are identified, and future opportunities are outlined.

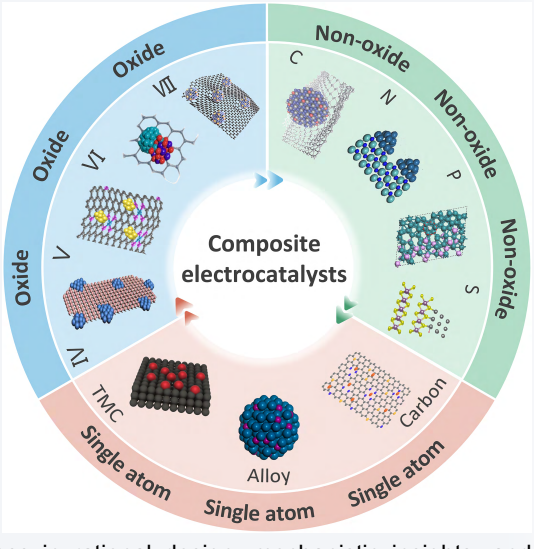

KEYWORDS: anion exchange membrane fuel cell, hydrogen oxidation reaction, composite electrocatalysts, single-atom catalysts, intermediate adsorption, interfacial water

1 Introduction

The fossil-fuel-dominated energy system has caused severe environmental damage, creating an urgent need for clean energy alternatives. Hydrogen, as a high-efficiency and zero-emission energy carrier, is regarded as a key enabler for the transition to a low-carbon energy infrastructure [1–3]. Fuel cells are central to efficiently utilizing hydrogen. Among them, proton exchange membrane fuel cells (PEMFCs) offer high energy efficiency but remain constrained by fluorinated membranes, and the heavy reliance of cathode on Pt-based catalysts [4, 5]. In contrast, anion exchange membrane fuel cells (AEMFCs) achieve significant potential cost advantages under alkaline conditions by combining non-noble-metal catalysts for the oxygen reduction reaction (ORR) with cost-effective membrane electrode assemblies (MEAs) [6, 7]. However, the hydrogen oxidation reaction (HOR) at anode of

Received: December 18, 2025; **Revised:** February 2, 2026
Accepted: February 10, 2026

✉Address correspondence to Siqi Lu, siqi_lu@126.com; Zhongbin Zhuang, zhuangzb@mail.buct.edu.cn

AEMFCs faces severe kinetic limitations in alkaline media. Compared with acidic conditions, the HOR rate of Pt-based catalysts in alkaline environments decreases by approximately two orders of magnitude [8]. This slowdown arises from multiple factors, including excessively strong hydrogen intermediate binding, enhanced adsorption of hydroxyl species, and higher energy barriers associated with water molecules. As a result, achieving sufficient anode kinetics necessitates increased Pt loadings, thereby diminishing the cost advantage of AEMFCs [9–11]. Moreover, under practical hydrogen feeds containing trace impurities (e.g., carbon monoxide (CO)) and during prolonged operation, AEMFC anodes suffer from severe catalyst poisoning and durability degradation, which further erode the techno-economic viability of the system [12, 13]. Therefore, the development of novel HOR electrocatalysts with high intrinsic activity, robust durability, and low noble-metal loading has become a central challenge for the technological advancement and commercial application of AEMFCs.

Currently, alkaline HOR catalysts are broadly divided into platinum-group metal (PGM) catalysts and non-PGM catalysts, the latter being predominantly nickel-based. In recent years, Ni-based catalysts have attracted growing attention owing to their earth abundance and low cost, and have achieved substantial progress through a series of interfacial and structural engineering strategies [14–17]. For example, *in situ* electrochemical surface reconstruction has been employed to construct Ni_3N–$Ni(OH)_2$ heterojunctions [18], pyrolysis-induced phase separation has been used to generate Ni–MoO_2 interfaces for electronic-structure modulation [19], and the fabrication of highly stable monolithic electrodes via an integrated hydrothermal corrosion–growth strategy [20]. These approaches effectively enhance HOR activity and have driven the performance of Ni-based catalysts toward that of Pt-based benchmarks. Notably, by optimizing charge distribution and stabilizing active sites through heterointerface engineering, key breakthroughs have also been achieved in improving the long-term durability of Ni-based catalysts. For instance, catalysts based on Ni–V_2O_3 heterostructures have demonstrated outstanding stability over up to 3000 potential cycles and during prolonged constant-potential operation [21]. Nevertheless, two ubiquitous bottlenecks still hinder the practical deployment of Ni-based catalysts: (i) Their activity remains inferior to that of state-of-the-art PGM catalysts, and (ii) when the potential exceeds ~ 0.1 V, Ni active sites are prone to oxidation, leading to performance decay. Consequently, despite their high cost, PGM catalysts are still regarded as the more practical choice due to their superior catalytic activity and resistance to oxidation [22, 23]. Accordingly, increasing the specific activity of PGM catalysts allows their loading to be reduced, which is essential for the commercialization of AEMFCs. However, the HOR mechanism in alkaline media is still not well understood, significantly hindering the rational design of catalysts. Developing PGM-based HOR electrocatalysts with high activity and durability remains a critical challenge for advancing AEMFC technology. Achieving this goal requires a thorough understanding of the reaction pathways and activity enhancement mechanisms. In alkaline media, the HOR generally proceeds through three elementary steps: Tafel (Eq. (1)), Heyrovsky (Eq. (2)), and Volmer (Eq. (3)) [24, 25]

$$\text{Tafel: } H_2 + 2^* \rightarrow 2H_{ad} \quad (1)$$

$$\text{Heyrovsky: } H_2 + OH^- + ^* \rightarrow H_{ad} + H_2O + e^- \quad (2)$$

$$\text{Volmer: } H_{ad} + OH^- \rightarrow H_2O + e^- + ^* \quad (3)$$

In the above equations, * denotes a hydrogen adsorption site on the catalyst, and H_{ad} represents an adsorbed hydrogen atom. The Tafel step involves the adsorption of H_2 without electron transfer. The Heyrovsky step involves the formation of H_{ad}, water, and electrons. The Volmer step corresponds to the desorption and discharge of H_{ad}. Whether the hydroxyl group adsorbs on the surface in the Heyrovsky and Volmer steps is still a matter of debate. The overall reaction pathway of the alkaline HOR can be summarized as either a Tafel–Volmer or Heyrovsky–Volmer mechanism, both of which involve the adsorption, transformation, and desorption of key intermediates, such as H, OH, and water molecules, at the electrode surface. Mechanistic studies of the alkaline HOR have therefore consistently focused on the behavior of these intermediates and their interactions with the catalyst surface. The field has evolved from early models emphasizing hydrogen binding energy (HBE) as a single descriptor to more comprehensive frameworks incorporating multiple parameters. The HBE theory establishes a "volcano" relationship between catalytic activity and hydrogen adsorption energy [26]. The bifunctional mechanism further introduces hydroxyl binding energy (OHBE), highlighting the synergistic reaction between H_{ad} and hydroxyl adsorption (OH_{ad}) at the interface [27]. More recently, researchers have revealed that the structure of interfacial water and the reorganization of its hydrogen-bonding network critically influence proton transport, and that OH_{ad} can act as a "water-structure catalyst" to optimize the double-layer environment and enhance reaction kinetics [28]. Although these mechanisms provide complementary insights into the origin of alkaline HOR activity, the complexity of the electrochemical interface and limitations of experimental techniques have prevented the establishment of a unified theoretical description to date, posing ongoing challenges for the rational design and performance optimization of catalysts.

Consequently, the development of PGM-based HOR electrocatalysts in alkaline conditions has proceeded in two stages: an early stage from single metals to alloys, followed by a current stage emphasizing composite structures. Noble metals (NMs), such as Pt, Pd, Ir, Ru, and Rh, exhibit exceptional intrinsic catalytic activity due to their placement within the optimal region of the "volcano plot" defined by HBE [29]. However, their high cost severely limits their large-scale application in fuel cells. In this context, alloying has emerged as a widely adopted and highly effective strategy for performance optimization. For example, Zhang et al. successfully synthesized self-supporting RhMo nanosheets with atomic-level thickness and a core–shell structure, achieving a mass activity of 6.96 $A \cdot mg_{Rh}^{-1}$ in alkaline HOR—21 times higher than commercial Pt/C [30]. Xue et al. developed a completely Pt-free Ru_7Ni_3/C catalyst, in which Ni alloying tunes the electronic structure of Ru, while surface Ni oxides facilitate water adsorption, significantly enhancing HOR performance [31]. The AEMFCs assembled with this catalyst reached a peak power density of 2.03 $W \cdot cm^{-2}$ under H_2/O_2 conditions, while substantially reducing catalyst cost. These studies indicate that the incorporation of a secondary metal can optimize the d-band structure of the primary metal via electronic tuning, thereby modulating the adsorption strength of key intermediates, such as H_{ad} and OH_{ad}.

Although alloy catalysts have achieved notable improvements in HOR performance, as single-phase materials, they struggle to simultaneously satisfy the diverse adsorption and desorption requirements of different intermediates across multiple elementary steps [32]. As a result, attention has shifted toward composite catalysts comprising two or more functional components. Such materials can induce interfacial structural distortion and charge redistribution, generating novel active sites that surpass the performance limits of single-component catalysts [33, 34]. Through rational design, composite electrocatalysts can exploit synergistic interactions among components, resulting in marked improvements in HOR activity and durability. Furthermore, as a unique and cutting-edge form of composite electrocatalysts, single-atom catalysts (SACs) disperse metal active centers at the atomic scale on tailored supports, constructing well-defined "metal–support" interfaces [35–37]. This approach not only maximizes noble metal atom utilization but also provides a precise platform to investigate how electronic modulation and microenvironment optimization jointly influence catalytic performance at the atomic scale.

Some reviews have discussed alkaline HOR electrocatalysts, mainly focusing on the metallic active centers and classifying the catalysts by the type of noble metal elements [11, 38, 39]. This review centers on composite catalysts for the alkaline HOR. Building on a systematic account of the alkaline HOR mechanism, the catalysts are categorized according to whether the material contains oxygen, dividing them into oxides and non-oxides. Special emphasis is placed on the relationships between the interfacial electronic structure and catalytic mechanisms at noble metal active sites. As illustrated in Fig. 1, the oxide section is organized by the periodic group of the constituent metal elements (e.g., Groups IVB, VB, VIB, and VIIB), while the non-oxide section covers emerging systems, such as carbides, nitrides, sulfides, and phosphides. By thoroughly analyzing the key mechanisms established at the interface between composite components and metal active sites—including interfacial interactions, oxygen vacancy (O_v) engineering, and directed electronic transfer—this review reveals their novel roles in synergistically modulating the adsorption energies of H, OH, and water, promoting hydrogen spillover, and enabling dynamic electronic mediation. These insights significantly expand the design space and performance limits of HOR electrocatalysts in alkaline conditions. Ultimately, by systematically reviewing the multifunctional roles and mechanistic evolution of various composite materials in Pt-, Ru-, and other noble-metal-based HOR catalysts, this work further incorporates single-atom catalysts into the overall discussion framework. Based on the tunable properties of different supports, these catalysts are classified into three categories: carbon-supported single atoms, single-atom alloys (SAAs), and transition metal compound-supported (TMC-supported) single atoms. Drawing on a comprehensive analysis of these material classes, this review aims to provide a solid theoretical foundation and material platform for the rational design of AEMFCs anode catalysts with high activity, enhanced stability, and low noble-metal loading.

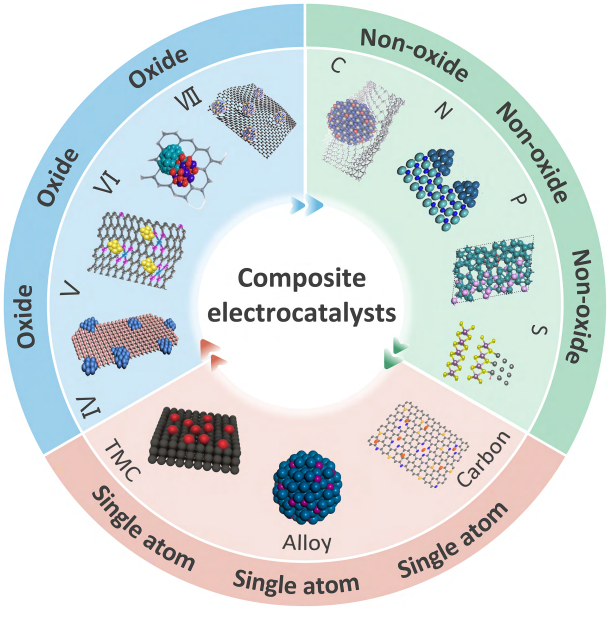

Figure 1 Schematic illustration for catalyst strategies of composite electrocatalysts for alkaline HOR.

2 Mechanism of the alkaline HOR

According to transition-state theory in chemical kinetics, the rate constant (k) of an elementary reaction can be expressed by the Eyring equation (Eq. (4)), under the assumption that a quasi-equilibrium is established between the reactants and the activated transition-state complex

$$k = \frac{\kappa k_B T}{h} \exp\left(-\frac{\Delta G^{\ddagger}}{RT}\right) = \frac{\kappa k_B T}{h} \exp\left(\frac{\Delta S^{\ddagger}}{R}\right) \exp\left(-\frac{\Delta H^{\ddagger}}{RT}\right) \quad (4)$$

where k_B is the Boltzmann constant, κ is the transmission coefficient, h is the Planck constant, R is the gas constant, and T is the absolute temperature. $\Delta G^{\ddagger}$ denotes the Gibbs free energy of activation and can be written as $\Delta G^{\ddagger} = \Delta H^{\ddagger} - T\Delta S^{\ddagger}$. Here, $\Delta H^{\ddagger}$ is the enthalpy of activation, which microscopically corresponds to the net energy required to break existing bonds and form new ones. It reflects the height of the reaction energy barrier and is directly influenced by the interaction strength between the electrocatalyst and reaction intermediates. By contrast, $\Delta S^{\ddagger}$ represents the entropy of activation and characterizes the degree of order in the transition state as well as the difficulty of microenvironmental reorganization during the reaction. In alkaline HOR kinetics, $\Delta S^{\ddagger}$ is particularly sensitive to the interfacial water structure, hydrogen-bonding networks, and proton-transfer pathways, all of which can be strongly modulated by the catalyst–electrolyte interface [40]. It should be noted that the state of interfacial water not only influences the ordering of the transition state but also alters the reaction energy barrier by modulating the adsorption strength and stability of intermediates.

Building on this theoretical framework, strategies for enhancing alkaline HOR activity can be systematically classified into two major categories: (i) Conventional electrocatalyst design approaches that optimize $\Delta H^{\ddagger}$ through tuning the adsorption energies of key reaction intermediates; and (ii) interfacial water structure engineering strategies that modulate the reorganization energy and intermediate adsorption states, thereby synergistically influencing both $\Delta S^{\ddagger}$ and $\Delta H^{\ddagger}$. This dual-parameter perspective offers a fundamentally new lens for understanding and improving HOR kinetics in AEMFCs (Fig. 2).

2.1 Optimizing intermediate adsorption

In the alkaline HOR, the adsorption behavior of key intermediates

on the catalyst surface directly governs both the activation energy barrier and the preferred reaction pathway. These intermediates primarily include hydrogen species (H) and hydroxyl species (OH) involved in the intrinsic reaction steps, as well as poisoning species, such as CO, originating from fuel impurities. As illustrated in Fig. 2, the following sections successively review the research progress and the gradual deepening of mechanistic understanding from three aspects: the HBE theory, the bifunctional theory and anti-CO poisoning strategies, and systematically elucidate their critical roles in governing alkaline HOR performance.

2.1.1 *HBE theory*

In the investigation of alkaline HOR mechanisms, the HBE theory is one of the earliest proposed and continues to be extensively discussed. This theory posits that the binding energy of adsorbed hydrogen on the catalyst surface serves as a key descriptor governing HOR activity in alkaline media. The origin of this concept can be traced to earlier investigations of the hydrogen evolution reaction (HER), which is the microscopic reverse process of HOR. Sheng et al. correlated the HBE values of a series of metals with their HER exchange current densities and constructed the classical Sabatier-type "volcano" plot, thereby revealing the universal significance of a moderately strong HBE for hydrogen electrocatalysis (Fig. 3(a)) [26]. Notably, this volcano relationship was established on the basis of HER data, because most non-noble metals are unstable at the working potentials of HOR, making it difficult to directly measure their HOR activities. Building upon this theoretical foundation, the same group subsequently focused on a single-metal model system and systematically investigated the electrochemical behavior of polycrystalline Pt over a wide pH range (0–13). For the first time, they experimentally uncovered a direct correlation among pH, HBE, and HOR activity: The HOR activity of Pt decreases with increasing pH, whereas its HBE increases linearly with pH [45]. These results unambiguously demonstrated the descriptor role of HBE in governing HOR kinetics within a single-metal system. To assess whether this descriptor possesses

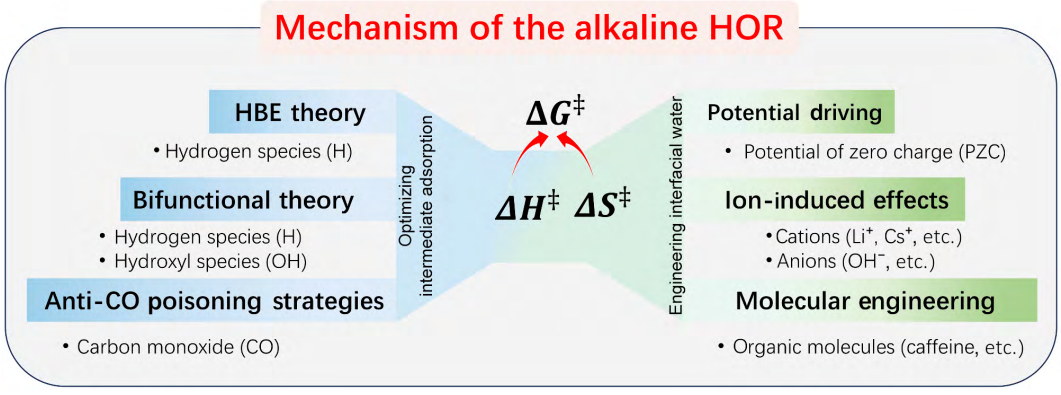

Figure 2 Schematic illustration for mechanism investigation and key governing factors for alkaline HOR.

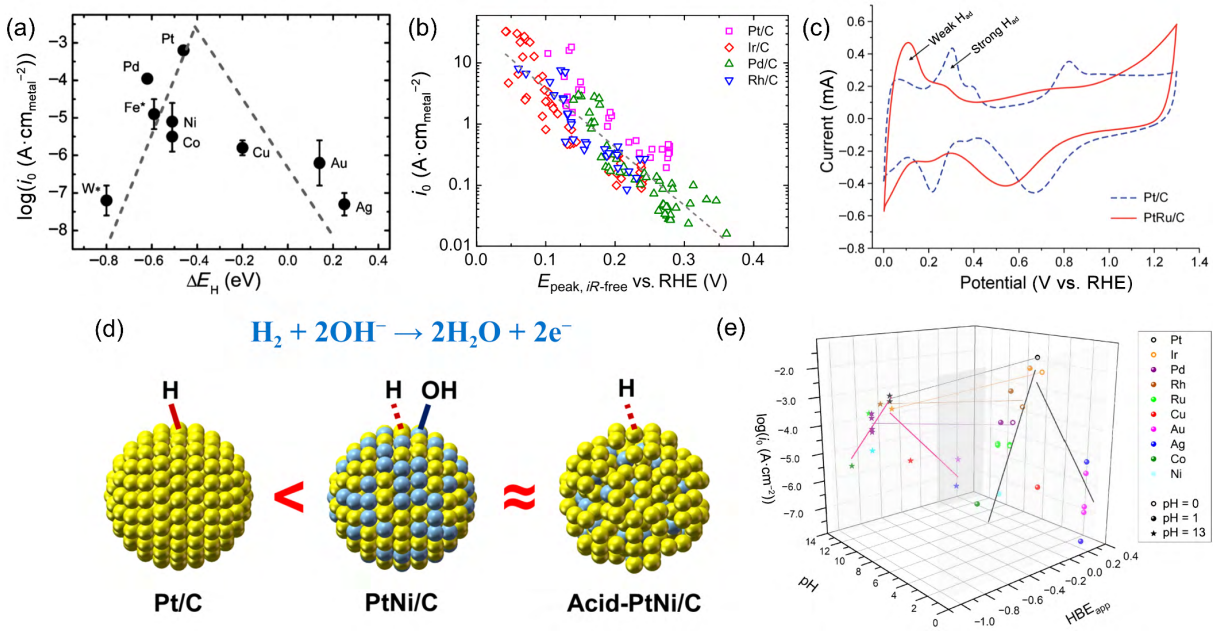

Figure 3 (a) Exchange current densities on monometallic surfaces plotted as a function of the calculated HBE. Reproduced with permission from Ref. [26], © The Royal Society of Chemistry 2013. (b) Correlation between the exchange current density of HOR/HER and H_{upd} desorption peak potential. Reproduced with permission from Ref. [41], © Zheng, J. et al. 2016. (c) Cyclic voltammetry curves of Pt/C and PtRu/C in deaerated 0.1 M KOH solution. Reproduced with permission from Ref. [42], © The Royal Society of Chemistry 2015. (d) Adsorption scheme of H_{ad} and OH_{ad} in Pt/C, PtNi/C, and acid-PtNi/C. Reproduced with permission from Ref. [43], © American Chemical Society 2017. (e) A schematic illustrating the research needed to establish HBE_{app} as the descriptor for HOR. Reproduced with permission from Ref. [44], © Zheng, J. et al. 2018.

cross-metal universality, Zheng et al. selected four platinum-group metals—Pt, Ir, Pd, and Rh—that remain stable over a broad pH range [41]. Their results showed that the linear increase of HBE with pH is a general trend shared by different metals, and that the HOR activities of all four metals exhibit a consistent negative correlation with HBE (Fig. 3(b)). These findings experimentally established HBE as a universal cross-metal descriptor for alkaline HOR, while simultaneously providing a systematic rebuttal of the OH adsorption-dominated mechanism. Zhuang and co-workers further supported this conclusion through CO-stripping experiments. Pt/C displays stronger oxophilicity than PtRu/C, yet exhibits inferior HOR activity. This finding suggests that OH adsorption is not the determining factor for HOR performance [42]. Instead, the superior activity of PtRu/C in alkaline media was attributed to electronic effects induced by Ru incorporation, which weakened hydrogen adsorption as clearly reflected in the cyclic voltammetry (CV) curves (Fig. 3(c)). To further validate the HBE theory, Zhuang and co-worker employed PtNi/C alloy nanoparticles (NPs) as model catalysts [43]. After acid treatment, the PtNi/C catalyst retained only hydrogen adsorption sites while removing surface OH adsorption sites, but its HOR activity remained unchanged. This result confirmed that the enhanced performance of alloy catalysts arises primarily from electronic modulation leading to weaker HBE, rather than from increased OH adsorption strength (Fig. 3(d)). Although these studies consistently highlight the central role of HBE in alkaline HOR, Yan and co-workers later introduced the concept of apparent HBE (HBE_{app}) based on the analysis of hydrogen underpotential deposition (H_{upd}) peaks [44]. They demonstrated that HBE_{app} is influenced not only by the intrinsic properties of the catalyst but also by the energy of water adsorption (Fig. 3(e)). The study revealed that relying solely on thermodynamic descriptors like HBE is insufficient to account for the reaction pathways and kinetic barriers in alkaline HOR, and provided guidance for developing more comprehensive theoretical models.

2.1.2 *Bifunctional theory*

In alkaline electrolytes, the high concentration of OH^- ions has prompted researchers to investigate the direct impact of interfacial OH_{ad} on reaction kinetics. The Markovic group demonstrated that depositing $Ni(OH)_x$ nanoclusters on Pt (111) surfaces significantly enhanced alkaline HOR activity, proposing a bifunctional mechanism: OH_{ad} and H_{ad} co-adsorb on the catalyst surface and subsequently combine upon desorption to form water molecules (Fig. 4(a)) [27]. This mechanism indicates that introducing oxophilic components to promote OH^- adsorption at the surface is a key strategy for enhancing alkaline HOR activity. Consequently, the OHBE was established as a second activity descriptor following HBE, both of which jointly govern the kinetics of alkaline HOR. To further verify the role of OH_{ad}, the Markovic group compared the HOR performance of $Pt_{0.5}Ru_{0.5}$ and $Pt_{0.1}Ru_{0.9}$ catalysts [46]. The latter, with higher Ru content and stronger oxophilicity, generated more OH_{ad} and exhibited double the HOR activity of the former, providing strong evidence for the critical role of OH_{ad} in promoting alkaline HOR (Fig. 4(b)). Koper and colleagues subsequently modified Pt (111) surfaces with various transition metals and observed a typical "volcano" relationship between alkaline HOR activity and OHBE, consistent with the Sabatier principle [47]. They further constructed a three-dimensional (3D) "volcano" plot combining HBE and OHBE, highlighting that high-performance alkaline HOR catalysts require moderate values of both descriptors (Fig. 4(c)). Building on these insights, Li and co-workers designed and synthesized Au@PtRu core–shell nanostructures, leveraging plasmonic enhancement from the Au core to enable *in situ* Raman monitoring of the HOR process on PtRu surfaces (Fig. 4(d)) [48]. A characteristic vibrational peak of OH_{ad} intermediates was clearly

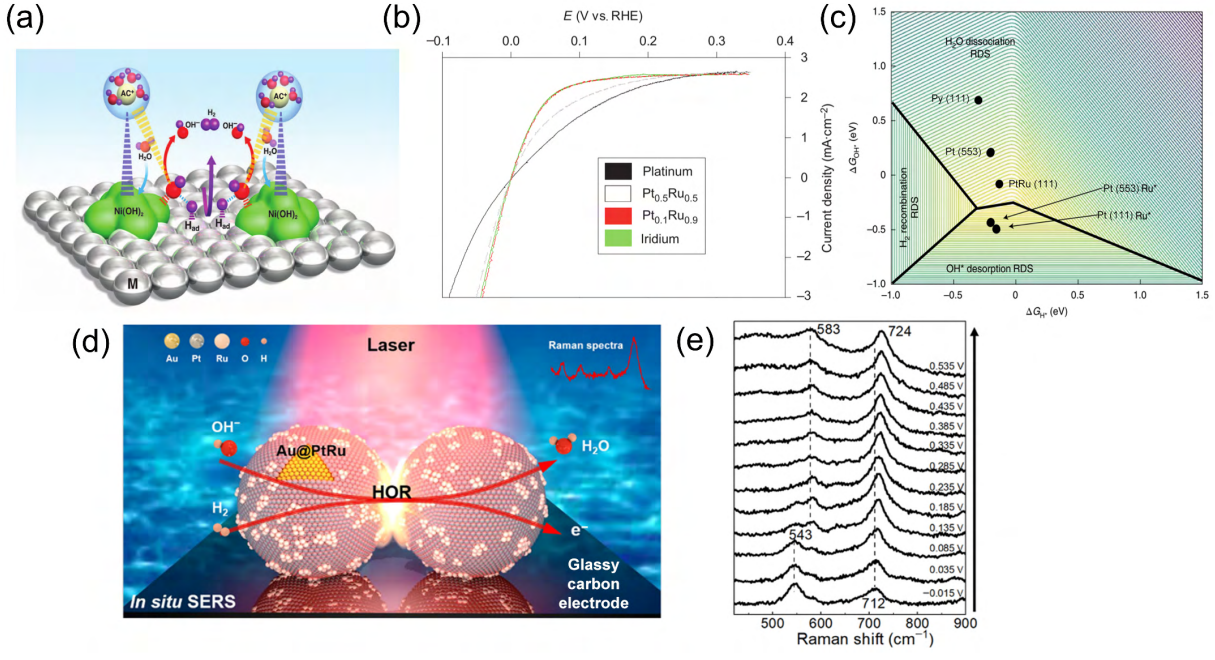

Figure 4 (a) Schematic representation of the HOR on $Ni(OH)_2$/Pt (111). Reproduced with permission from Ref. [27], © American Association for the Advancement of Science 2011. (b) HOR/HER polarization curves for Pt-poly (black curves) and PtRu alloys with 50% Ru (dashed grey) and 90% Ru (dashed red). Reproduced with permission from Ref. [46], © Springer Nature Limited 2013. (c) 3D activity volcano for catalyst design. Reproduced with permission from Ref. [47], © McCrum, I. T. et al. 2020. (d) Schematic illustration of the Au@PtRu core–shell nanoparticle-enhanced Raman spectroscopy for an *in situ* alkaline HOR study on PtRu surfaces. (e) *In situ* enhanced Raman spectra of HOR catalyzed by $Au@Pt_1Ru_{0.2}$ NPs. Reproduced with permission from Ref. [48], © American Chemical Society 2022.

detected at 712 cm^{-1}, with signal intensity closely correlating with reaction current changes (Fig. 4(e)). This result provided the first direct spectroscopic evidence that OH_{ad} acts as a key intermediate in alkaline HOR, demonstrating that its efficient generation and stable adsorption markedly facilitate interfacial coupling with H_{ad}, significantly enhancing the hydrogen oxidation reaction rate in the Volmer step under alkaline conditions.

2.1.3 *Anti-CO poisoning strategies*

For the HOR, the HBE theory and the bifunctional theory rationalize catalyst activity regulation from the perspectives of H and OH adsorption, respectively, thereby capturing the fundamental roles of two key reaction intermediates. However, under practical operating conditions of AEMFCs, hydrogen is often supplied from cost-effective reforming processes (e.g., steam methane reforming), which unavoidably introduce CO impurities, typically in the range of 100 ppm to 3% [49]. These CO molecules compete with H for adsorption on catalytic active sites and can even completely occupy them, leading to catalyst poisoning and deactivation, thereby severely degrading cell performance and durability. Even CO concentrations as low as 10 ppm are sufficient to markedly suppress the HOR activity of noble-metal catalysts represented by Pt [39]. Therefore, developing anode catalysts with high CO tolerance is not only critical for improving the operational stability of AEMFCs under realistic conditions but also constitutes a key technological pathway toward their commercial deployment. Pt-based catalysts are particularly vulnerable to CO poisoning, which fundamentally originates from the exceptionally strong chemisorption of CO on Pt surfaces. This adsorption arises from pronounced electronic interactions between CO and Pt: CO donates electrons to the Pt 5d orbitals, while Pt back-donates electrons into the CO 2π* antibonding orbitals, thereby forming a highly stable Pt–CO bond [50]. In addition, the actual anode operating potential for HOR is typically below 0.1 V vs. reversible hydrogen electrode (RHE) (V_{RHE}) [51]. At such low potentials, Pt surfaces can neither efficiently dissociate water to generate sufficient OH^- species for CO oxidation, nor reach the potential required for the direct electrochemical oxidation of CO (> 0.3 V) [49, 52]. Consequently, once CO is strongly adsorbed on Pt sites, no effective self-removal pathway exists under device operating conditions, resulting in essentially irreversible poisoning of the active sites.

To address the pronounced susceptibility of anode catalysts to CO poisoning in AEMFCs, current research efforts have primarily focused on two strategic directions: "reducing CO adsorption" and "accelerating CO removal". The first strategy involves tuning the electronic structure of active metals to weaken the metal–CO bond strength (electronic effect). For example, Dong et al. employed a synergistic cascade design combining a Fe–N–C support with a PtNiMo alloy to attenuate Pt → CO back-donation (Fig. 5(a)), thereby endowing the PtNiMo/Fe–N–C catalyst with outstanding CO tolerance [13]. After continuous operation for 2000 s in 1000 ppm CO/H_2, the HOR activity of this catalyst could still be maintained above 80% (Fig. 5(b)). Similarly, Zhou et al. constructed a $Ru@TiO_2$ lattice-confined architecture and significantly suppressed CO adsorption by downshifting the d-band center [53] (Fig. 5(c)). The second strategy relies on introducing oxophilic components to construct bifunctional interfaces that promote CO oxidation and removal (bifunctional effect). For instance, Huang and co-workers incorporated Pb into RuCu nanoflowers (NFs), where Pb served as oxygen-rich sites to enhance OH adsorption and facilitate CO oxidation, enabling the catalyst to retain high activity even under CO-containing atmospheres [54] (Fig. 5(d)). In another representative example, Zhang et al. designed Ru-CrO_x Janus-type cluster heterostructures, in which interfacial electronic reconstruction allowed Ru and CrO_x to preferentially optimize H desorption and OH adsorption, respectively. As a result, this

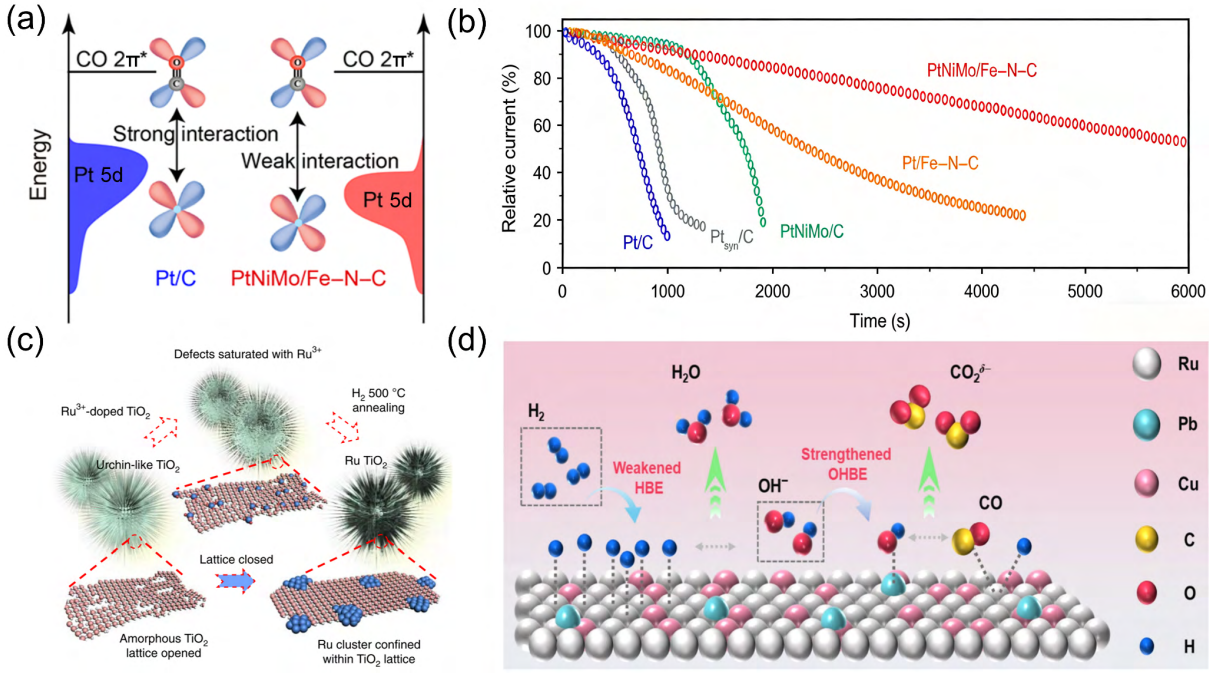

Figure 5 (a) Scheme for mitigating electron back donation in PtNiMo/Fe–N–C. (b) Chronoamperometric response of PtNiMo/Fe–N–C in 1000 ppm CO/H_2. Reproduced with permission from Ref. [13], © American Chemical Society 2023. (c) Lattice evolution during production of lattice-confined $Ru@TiO_2$. Reproduced with permission from Ref. [53], © Zhou, Y. Y. et al. 2020. (d) Schematic illustration of alkaline HOR over Pb_x-$Ru_{92}Cu_8$ NFs. Reproduced with permission from Ref. [54], © Wiley-VCH GmbH 2023.

catalyst simultaneously achieved ultrahigh HOR activity together with exceptional CO tolerance and operational stability [55].

2.2 Engineering interfacial water

At the electrochemical interface, reaction kinetics are governed not only by $\Delta H^{\ddagger}$, which is primarily determined by the adsorption energies of surface intermediates on the catalyst, but also strongly influenced by the structure and dynamic properties of the interfacial water environment. Key descriptors of this microenvironment—including molecular orientation, hydrogen-bond network connectivity, as well as its degree of dynamical flexibility or rigidity—collectively define the interfacial water characteristics and modulate the reaction energy barrier by stabilizing the transition state, while simultaneously constraining the order and energetic cost of solvent reorganization. Together, these effects determine both $\Delta H^{\ddagger}$ and $\Delta S^{\ddagger}$ of the overall reaction process [40]. Notably, these interfacial water characteristics are not static but respond sensitively to external electrochemical conditions. In this context, the electrode potential and the electrolyte composition—encompassing cations, anions, and functional additive molecules—represent two key external tuning parameters that can actively reconstruct the microscopic state of interfacial water, thereby modulating reaction pathways and rates [56].

Therefore, developing a fundamental understanding of interfacial water structure and achieving its rational regulation has emerged as a new paradigm for overcoming the kinetic bottleneck of the alkaline HOR. In this section, we first outline the intrinsic characteristics of interfacial water structure, and then systematically discuss how three external strategies—potential-driven regulation, ion-induced modulation, and molecular engineering—govern alkaline HOR kinetics by tailoring the interfacial water environment.

2.2.1 Intrinsic structure of interfacial water and hydrogen-bond networks

A water molecule consists of two hydrogen atoms and one oxygen atom covalently bonded into a bent (V-shaped) geometry with a bond angle of approximately 104.5° (Fig. 6(a)) [57]. This intrinsic molecular geometry, together with the relatively large dipole moment of water, gives rise to pronounced orientational ordering under the strong electric field at an electrode surface. As a consequence, the structure of interfacial water differs markedly from that of bulk water. Using X-ray absorption spectroscopy (XAS), Velasco-Velez et al. probed the structure of water adjacent to a gold electrode and revealed that nearly 50% of the interfacial water molecules adopt a "flat-lying" configuration parallel to the surface [58]. To further quantify such orientational behavior, Li et al. employed first-principles molecular dynamics simulations and defined the orientation of interfacial water by the angle (θ) between the molecular plane and the surface normal (z-axis). Two dominant configurations were identified: When θ lies between 0° and 60°, the molecule adopts an "H-up" configuration, in which the oxygen atom points toward the electrode surface; when θ lies between 120° and 180°, the molecule adopts an "H-down" configuration, in which the hydrogen atoms point toward the surface (Fig. 6(b)) [59]. The orientation of individual water molecules not only determines their own interfacial arrangement but also directly regulates the geometry and connectivity between neighboring molecules through hydrogen bonding. Such hydrogen-bonding interactions originate from the large electronegativity difference between hydrogen and oxygen (2.20 vs. 3.44), which imparts partial positive charge (δ^+) to hydrogen atoms and partial negative charge (δ^-) to oxygen atoms. As a result, the δ^+ hydrogen of one molecule is electrostatically attracted to the lone-pair electrons on the δ^- oxygen of a neighboring molecule, forming a hydrogen bond.

Hydrogen bonds are highly directional, approximately aligned along the O–H bond axis, and exhibit saturation behavior: Each water molecule can, in principle, act as both a proton donor and a proton acceptor to form up to two hydrogen bonds of each type, enabling a maximum of four hydrogen bonds in a tetrahedral coordination motif (Fig. 6(c)) [57]. Through such interactions, water molecules self-assemble into two- or three-dimensional hydrogen-bond networks at the electrode/electrolyte interface. The connectivity of these networks—namely, the continuity and integrity of hydrogen-bond pathways—directly governs mass transport and charge-transfer processes [60, 61]. It should be emphasized that hydrogen-bond saturation does not imply that all four bonding sites are fully occupied at all times. Using Raman spectroscopy to analyze O–H stretching frequencies, Sun and co-workers classified interfacial water molecules into three categories according to their actual hydrogen-bond coordination states: free O–H groups (no hydrogen bond, ~ 3600 cm^{-1}), three-coordinated water molecules (liquid-like structure, ~ 3400 cm^{-1}), and four-coordinated water molecules (ice-like structure, ~ 3200 cm^{-1}) [62]. These water molecules are not statically arranged. Their relative positions, orientations, and coordination states continuously fluctuate, leading to persistent breaking and reformation of hydrogen bonds. This dynamic nature enables hydrogen-bond networks to respond sensitively to the surrounding chemical environment and external perturbations, thereby modulating the solvent reorganization energy [63]. Specifically, the lower the energetic cost for water molecules to rearrange around a reaction intermediate, the smaller the reaction barrier and the faster the kinetics. In contrast, when interfacial water molecules are strongly anchored by intense electric fields or interact strongly with specific ions, their mobility becomes restricted, and the hydrogen-bond network exhibits increased rigidity. Under such conditions, solvent reorganization becomes difficult, resulting in a pronounced retardation of reaction kinetics [64, 65].

2.2.2 Potential-driven regulation and electric-field reconstruction

The electrode potential can directly regulate the structure of interfacial water by altering the strength of the interfacial electric field. The key physical parameter governing this effect is the potential of zero charge (PZC), defined as the electrode potential at which the surface carries no excess charge [66]. Using laser-induced temperature-jump techniques, Garcia-Araez et al. and Ledezma-Yanez et al. measured the PZC of the Pt (111) surface to be approximately 0.37 V_{RHE} in acidic media [66], whereas it shifts positively to about 0.70 V_{RHE} in alkaline media [65]. Rebollar et al. further pointed out that, with increasing pH, the potential difference between the HOR operating potential and the PZC progressively increases, indicating that the electrode surface accumulates a higher density of negative charge under alkaline conditions and thus generates a stronger interfacial electric field (Fig. 6(d)) [67]. This intensified electric field forces interfacial water molecules to preferentially adopt the "H-down" configuration and drives the hydrogen-bond network toward a highly ordered and increasingly rigid structure. Such an ordered and rigid interfacial water layer severely impedes mass transport processes and

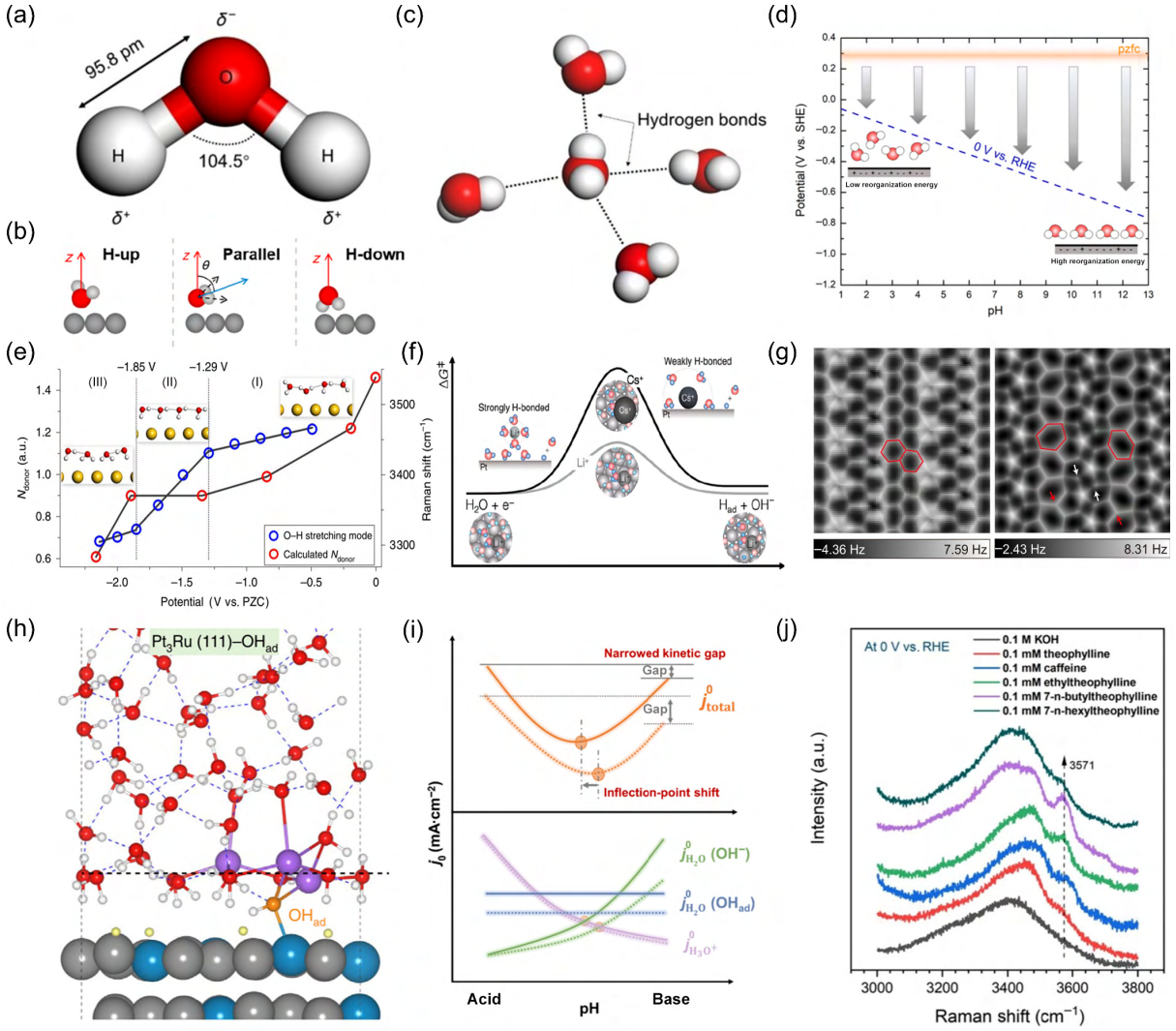

Figure 6 (a) The atomic structure and charge distribution of a water molecule. ((a) and (c)) Reproduced with permission from Ref. [57], © Wiley-VCH GmbH 2025. (b) Schematic diagram of the interfacial water structures with different orientations. Reproduced with permission from Ref. [59], © American Chemical Society 2022. (c) Tetrahedral hydrogen-bonding structure between water molecules. (d) Pourbaix diagram showing the pH dependence of the hydrogen equilibrium potential (0 V vs. RHE), the effective potential of zero free charge (pzfc) of Pt (111), and the water orientation and reorganization energy at the electrode/electrolyte interface. Reproduced with permission from Ref. [67], © American Chemical Society 2020. (e) Potential-dependent evolution of the hydrogen-bond network of interfacial water. The atomic structure and charge distribution of a water molecule. Reproduced with permission from Ref. [68], © Li, C. Y. et al. 2019. (f) Cation effect on energy barrier and interfacial water distribution in reaction process. Reproduced with permission from Ref. [69], © Huang, B. T. et al. 2021. (g) Simulated AFM images comparing the water structures atop Li^+ (left) and Cs^+ (right). Reproduced with permission from Ref. [70], © Tian, Y. et al. 2024. (h) Representative snapshots of the AIMD-simulated interface structures on a Pt_3Ru (111) electrode with OH adsorption. Reproduced with permission from Ref. [61], © Li, P. et al. 2022. (i) Schematic illustration of the triple-path model. Reproduced with permission from Ref. [71], © American Chemical Society 2023. (j) Raman spectra of interfacial water on a pc Pt electrode in 0.1 M KOH with 0.1 mM various theophylline derivatives at 0 V. Reproduced with permission from Ref. [72], © Wiley-VCH GmbH 2022.

ultimately leads to a substantial slowdown of HOR kinetics under alkaline conditions. Consistent conclusions were reached by Li et al. through a combination of *ab initio* molecular dynamics (AIMD) simulations and *operando* electrochemical Raman spectroscopy. They demonstrated that when the interfacial potential approaches the PZC, a more continuous and complete hydrogen-bond network can be established, which facilitates proton transfer across the interface (Fig. 6(e)) [68].

2.2.3 *Ion-induced effects and interfacial hydration*

As an excellent solvent, water readily dissolves electrolytes to form ions. The local electric fields generated around these ions attract polar water molecules, inducing their accumulation and orientational ordering to form hydration layers with distinct structural motifs that differ markedly from those in the bulk solution [73]. However, the mechanistic role of electrolyte cations in regulating the interfacial hydrogen-bond network has long remained controversial: Do cations enhance or disrupt the ordering of interfacial water? To address this question, the Shao-Horn team systematically investigated the effects of alkali metal cations (Li^+, Na^+, K^+, Rb^+, and Cs^+) on HOR kinetics over a wide pH range. They found that HOR activity increases monotonically with the structure-forming ability of the cations, following the order $Cs^+ < Rb^+ < K^+ < Na^+ < Li^+$, accompanied by a decrease in solvent reorganization energy. Among them, Li^+ exhibits the lowest reorganization energy and the fastest kinetics. Acting as a structure-forming ion, Li^+

stabilizes a more complete interfacial hydrogen-bond network and increases the local density of interfacial water molecules, thereby enhancing HOR activity. In contrast, Cs^+ behaves as a structure-breaking ion; through strong ion–surface interactions, it expels water molecules from the interface, distorts the hydrogen-bond network, and consequently suppresses HOR kinetics (Fig. 6(f)) [69]. To validate this mechanism at the atomic scale, the same team further employed scanning tunneling microscopy (STM) and noncontact atomic force microscopy (AFM) to directly visualize interfacial water structures on a charged Au (111) surface in the presence of different alkali metal cations [70]. Remarkably, Li^+ was observed to be lifted away from the surface by surrounding water molecules, forming an ice-like hexagonal water layer between the ion and the electrode. In contrast, K^+ and Cs^+ were found to be in direct contact with the electrode surface, leading to pronounced distortions of the hydrogen-bond network (Fig. 6(g)). These striking structural differences provide direct and real-space evidence that cations regulate reaction kinetics by altering the molecular arrangement of interfacial water, and they mark a critical transition in the field from macroscopic kinetic measurements to microscopic, *in situ* visualization of interfacial structures.

Beyond electrolyte cations, the adsorption behavior of interfacial anions—particularly OH^-—also plays a decisive role in regulating hydrogen-bond networks. Chen and co-workers combined AIMD simulations with surface-enhanced infrared spectroscopy and revealed that, in alkaline media, Na^+ accumulates near the Pt surface, creating a hydrogen-bond network gap of approximately 4.26 Å at the reaction interface, which severely hinders proton transport during the alkaline HOR [61]. To resolve this bottleneck, the authors employed a Pt_3Ru alloy as a model catalyst and exploited the preferential adsorption of OH^- on Ru sites to intentionally coordinate OH^- with the accumulated Na^+. This strategy successfully liberated the trapped water molecules and reconstructed a continuous hydrogen-bond channel across the interface (Fig. 6(h)). This work not only proposed, for the first time, the "connectivity of the hydrogen-bond network" as a central descriptor for rationalizing the kinetic disparity between acidic and alkaline HOR, but also, more importantly, demonstrated a complete experimental logic from "gap identification" to "directed repair". It thus elucidated the dynamic regulatory role and mechanistic function of OH^- adsorption in interfacial water structure. Building on these findings, the same team further explored the HOR kinetics of Pt, Rh, Ru, and their phosphides over a wide pH range [71]. They observed that all catalysts exhibit a pH-dependent kinetic inflection point that correlates strongly with the strength of OH^- adsorption: the stronger the OH^- adsorption, the more the inflection point shifts toward lower pH values, and the smaller the activity gap between acidic and alkaline conditions. By constructing a microkinetic model incorporating three pathways—H_3O^+, H_2O/OH^-, and H_2O/OH_{ad}—the authors demonstrated that OH^- does not primarily regulate the intrinsic surface reaction barrier. Instead, it enhances hydrogen-bond network connectivity through a ternary "anion–cation–water" synergy. This conclusion generalizes the interfacial water–structure mechanism from a specific catalyst system to a broad range of materials and promotes hydrogen-bond-network engineering as a universal design principle in electrocatalysis (Fig. 6(i)).

2.2.4 *Molecular engineering and microenvironment design*

Beyond the intrinsic ions present in electrolytes, exogenously introduced functional organic molecules can also actively regulate the interfacial water environment. For example, Intikhab et al. discovered that caffeine molecules form a self-limiting adsorption layer on Pt surfaces. Owing to their hydrophobic backbone, these molecules attenuate the interfacial electric field and reduce the solvent reorganization energy, leading to a 5–7 fold increase in the exchange current density of the alkaline HOR [74]. To deconvolute the molecular origin of caffeine's activity, Zhao et al. synthesized a series of structurally analogous 7-alkylxanthine derivatives. *Operando* Raman spectroscopy revealed that, with increasing alkyl-chain length, the intensity of the ~ 3587 cm^{-1} band—assigned to weakly hydrogen-bonded water—first increases and then decreases, mirroring the volcano-type trend in alkaline HOR activity (Fig. 6(j)) [72]. Molecular dynamics simulations further showed that the alkyl chains act as "structure breakers", effectively disrupting overly rigid hydrogen-bond networks at the interface and thereby enhancing reaction kinetics. However, when the alkyl chains become excessively long ($C \geq 6$), the hydrophobic moieties form a mass-transport barrier that counteracts the beneficial effect, resulting in a decline in activity. Subsequently, the same team extended the spatial scope of "molecular regulation" into the bulk region and found that tetrapropylammonium (TPA^+) can induce the formation of long-range hydrogen-bond chains in interfacial water, thereby enhancing proton structural diffusion and accelerating alkaline HOR kinetics. These studies collectively demonstrate that rational molecular design to tune the rigidity and connectivity of interfacial hydrogen-bond networks has emerged as a powerful paradigm for actively programming the reaction microenvironment [75].

Taken together, mechanistic understanding of the alkaline HOR has evolved from the traditional binary "catalyst surface–intermediate" model toward a dynamic ternary framework comprising the "catalyst–intermediate–interfacial water". The adsorption states and reaction pathways of key intermediates, such as H, OH, and CO, are not governed solely by their intrinsic bonding to the metal surface, but are simultaneously and strongly modulated by their surrounding hydration shells and the interfacial hydrogen-bond network. On the one hand, water molecules directly stabilize or destabilize specific intermediate configurations through hydration layers. On the other hand, the connectivity and dynamicity of the hydrogen-bond network fundamentally determine the efficiency of proton transfer and the magnitude of the solvent reorganization barrier. Nevertheless, due to the complexity and multi-scale coupling of electrochemical interfaces, no unified theoretical framework yet exists that can fully account for HOR behavior under alkaline conditions. Despite this, these studies have collectively advanced our understanding of interfacial processes in alkaline HOR from multiple perspectives, providing a solid foundation for the rational design of high-performance catalysts.

3 Characterization and testing methods

To validate mechanistic hypotheses of the alkaline HOR and to enable quantitative evaluation of anode catalyst performance, systematic experimental characterization and testing are indispensable. This section presents key methodologies from two complementary levels: (i) *in situ* observations at the atomic and molecular scales and (ii) system-level performance assessment. The former aims to directly capture the structural evolution of catalyst surfaces and the behavior of reaction intermediates under working

conditions, whereas the latter establishes a complete testing framework spanning from idealized model systems to practical devices, thereby enabling comprehensive evaluation of both intrinsic activity and overall output performance.

3.1 Mechanistic characterization methods

Conventional electrochemical techniques—for example, inferring intermediate adsorption behavior from potential shifts of characteristic peaks in cyclic voltammograms (Fig. 7(a)) [45], or determining the potential of zero charge via laser-induced potential-jump measurements [66]—can provide valuable macroscopic information. However, they remain insufficient for real-time, atomic- or molecular-level resolution of interfacial electrochemical processes. To overcome these limitations, a range of *in situ* characterization techniques has been developed, enabling direct visualization of the dynamic structural evolution of catalysts under operating conditions.

Microscopy and diffraction techniques play a central role in monitoring atomic and molecular processes occurring at catalyst surfaces in real time. STM and noncontact AFM provide atomic-resolution images in real space. The former is sensitive to surface electronic states and can directly visualize electrolyte-induced surface reconstruction and the dynamic processes of ion adsorption (Fig. 7(b)), whereas the latter is sensitive to interatomic forces and enables precise identification of chemical species, visualization of hydrogen-bond networks, and determination of three-dimensional molecular orientations. When used in combination, these two techniques offer intuitive insights into the distinct hydration structures induced by different alkali metal cations (e.g., Li^+ versus Cs^+) on electrode surfaces [70]. Surface X-ray diffraction and crystal truncation rod (CTR) analysis provide complementary, ensemble-averaged structural information (Fig. 7(c)) [76]. For example, CTR measurements clearly distinguish that Li^+ promotes the formation of a compact hydration layer on Pt (110), whereas Cs^+ induces a bilayer-like structure, the latter of which hinders the adsorption of key reaction intermediates [77]. Beyond monitoring surface structure, dynamic tracking of key reaction intermediates constitutes another critical link between atomic-scale interfacial structure and macroscopic reaction kinetics. Vibrational spectroscopic techniques exhibit unique advantages in this context. Surface-enhanced infrared absorption spectroscopy (SEIRAS) probes the O–H stretching vibrations of interfacial water molecules and can sensitively distinguish different hydrogen-bonded water species (Fig. 7(d)) [61]. It thus directly reflects the connectivity of hydrogen-bond networks and their regulatory role in reaction kinetics. Surface-enhanced Raman spectroscopy (SERS)—particularly when implemented using shell-isolated nanoparticle (SHIN)-enhanced Raman spectroscopy (SHINERS)—exploits localized electromagnetic field enhancement (Fig. 7(e)) to enable *in situ* tracking of potential-dependent configurational changes of water molecules on atomically flat electrode surfaces [68]. Together, these vibrational spectroscopic techniques provide critical, bond-level insights into how the interfacial microenvironment governs reaction pathways and electrocatalytic performance.

3.2 Performance evaluation methods

Mechanistic investigations are ultimately intended to guide the rational design of high-performance electrocatalysts and must be validated through systematic performance evaluation. The assessment of HOR catalysts is inherently a multidimensional and nontrivial task, as no single metric or method can comprehensively

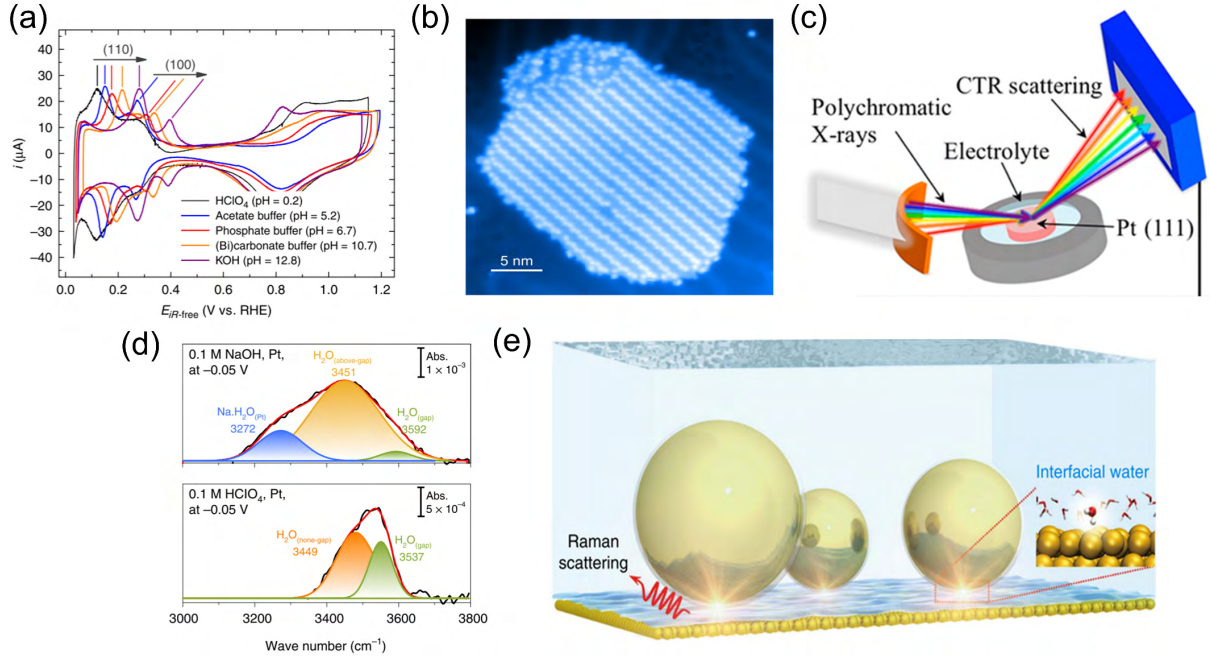

Figure 7 (a) Steady state CVs of Pt collected in selected Ar-saturated electrolytes at a sweep rate of 50 $mV \cdot s^{-1}$ in a full range of solution pH. Reproduced with permission from Ref. [45], © Springer Nature Limited 2015. (b) Constant-current STM image of two-dimensional (2D) Cs^+-water layer on Au (111). The 2D Cs^+-water layer is composed of single-stranded zigzag Cs^+ chains. Reproduced with permission from Ref. [70], © Tian, Y. et al. 2024. (c) Schematic illustration of the *in situ* wavelength-dispersive X-ray CTR scattering measurement of the Pt (111) electrode surface. Reproduced with permission from Ref. [76], © American Chemical Society 2017. (d) Deconvoluted infrared spectra showing the O–H stretching vibration at −0.05 V (vs. RHE) in NaOH (top) and $HClO_4$ (bottom) solutions. Reproduced with permission from Ref. [61], © Li, P. et al. 2022. (e) Schematic illustration of the Au SHINs-single-crystal surface coupling mode, in which "hot spots" of the electric field largely enhance the Raman signals of water at the interface. Reproduced with permission from Ref. [68], © Li, C. Y. et al. 2019.

reflect their overall performance. Accordingly, catalyst evaluation must simultaneously consider intrinsic activity, practical output capability, and long-term durability. To this end, two complementary testing platforms have been established in the field: (i) Model studies based on the rotating disk electrode (RDE) technique and (ii) device-level validation based on AEMFCs. These two approaches operate at the mechanistic and application-oriented levels, respectively, and together constitute a complete performance-evaluation chain for HOR electrocatalysts.

For probing intrinsic catalytic activity and elucidating reaction mechanisms, the RDE platform serves as an idealized and highly controllable laboratory model system. By decoupling many of the complex perturbations present in practical fuel cells, it enables focused study of the electrochemical behavior occurring at catalyst surfaces. The core evaluation parameters in RDE measurements include the electrochemically active surface area (ECSA), kinetic descriptors, such as the exchange current density and kinetic current density, as well as auxiliary metrics, including the Tafel slope and mass activity. Collectively, these parameters quantify both the "number of effective active sites" and the "intrinsic reaction efficiency" of a given catalyst. They can be quantitatively interpreted using classical formalisms, such as the Butler–Volmer and the Koutecky–Levich equations [10, 11]. However, the RDE testing environment differs fundamentally from that of a real fuel cell in terms of interfacial structure, mass-transport processes, and the three-phase boundary. In particular, in acidic media, the HOR becomes severely limited by hydrogen mass transport, rendering conventional RDE measurements ineffective unless supplemented by hydrogen-pump techniques. These intrinsic limitations highlight the necessity of coupling RDE studies with device-relevant conditions [11, 24].

To evaluate catalyst performance under realistic operating conditions, AEMFC testing is indispensable. This platform closely mimics practical working environments and, therefore, serves as the definitive benchmark for validating the comprehensive performance of HOR electrocatalysts. The core performance metrics are derived from polarization curves and power-density curves, with particular emphasis placed on the peak power density, the power density at a specified cell voltage (e.g., 0.65 V), and the noble-metal loading [39]. Beyond short-term output characteristics, long-term durability tests are routinely conducted to assess catalyst stability, tolerance to poisoning, and compatibility with other MEA components [78, 79]. It should be emphasized that AEMFC performance is highly sensitive to MEA fabrication protocols, operating-condition control, and system activation procedures. Consequently, the measured results directly reflect the practical potential and durability of the catalyst [80–82].

Although RDE and AEMFC tests differ substantially in terms of reaction environment, mass-transport characteristics, and interfacial structure, the two platforms can be rationally coupled through methodological refinement and cross-validation. More broadly, by integrating multi-scale and multidimensional approaches—from microscopic *in situ* characterization to macroscopic device-level testing—it becomes possible to construct a closed-loop understanding that links atomic structure, interfacial processes, and practical performance. In the following sections, we will focus on high-performance alkaline HOR electrocatalysts, with an emphasis on composite catalyst systems. Guided by the above-described characterization and testing frameworks, we will systematically elucidate their materials-design principles, catalytic mechanisms, and ultimate performance metrics.

4 Recent advances of composite catalysts for alkaline HOR

To address the dual challenges of sluggish alkaline HOR kinetics and the high cost of noble-metal catalysts, the development of electrocatalysts with high activity, excellent stability, and low platinum loading has become a central research focus. In recent years, the design of alkaline HOR electrocatalysts has undergone a marked transition from single-phase alloys to multicomponent composites. Compared with conventional alloys, composite catalysts—by constructing functionalized interfaces and introducing synergistic effects—not only enable precise tuning of intermediate adsorption behaviors, but also overcome the inherent limitation of single-phase alloys in simultaneously accommodating diverse adsorption/desorption requirements during the reaction, thus offering new material platforms and design strategies for enhancing HOR performance. In this chapter, composite catalysts are systematically categorized into oxides and non-oxides, depending on whether the secondary component contains oxygen. The oxide-based systems are further organized according to the periodic group of the constituent elements (e.g., IVB, VB, VIB, and VIIB), whereas the non-oxide category encompasses diversified families, such as carbides, nitrides, sulfides, and phosphides. All catalysts discussed, along with their alkaline HOR activities, are summarized in Table 1 for systematic comparison and performance analysis.

4.1 Oxide components

4.1.1 IVB-group transition metal oxides (TiO_2 and ZrO_2)

Among IVB transition metal oxides, TiO_2 and ZrO_2 have emerged as crucial materials for addressing the high-potential activity decay of Ru-based HOR catalysts, owing to their tunable redox properties, abundant oxygen vacancy defects, and excellent interfacial electron transfer with metals. Jiang et al. developed a Ru catalyst (IO-Ru-TiO_2/C) constructed via a TiO_2-based interfacial oxidation strategy (Fig. 8(a)) [83]. The catalyst enables interfacial electron transfer from Ru to TiO_2, tuning the Ru oxidation state toward Ru^{4+} and producing a nearly half-filled d orbital configuration. Since the half-filled d orbital lacks electrons available for oxidation, the catalyst exhibits outstanding resistance to oxidative degradation while simultaneously weakening OH^- adsorption on Ru sites. These synergistic effects endow IO-Ru-TiO_2/C with excellent HOR activity under alkaline conditions (Figs. 8(b) and 8(c)). In contrast to Jiang's interfacial oxidation approach, Zhou et al. employed a unique lattice-confinement strategy to construct Ru clusters confined within sea-urchin-like TiO_2 crystals (Ru@TiO_2) [53]. Amorphous TiO_2 undergoes crystallization during H_2 annealing, forming atomically bonded Ru–Ti interfaces. This intimate bonding promotes electron transfer from TiO_2 to Ru clusters, increasing the 4d orbital electron occupancy and rendering Ru in an electron-rich state. The resulting electronic structure imparts dual benefits: suppression of CO adsorption and moderated adsorption energies of both H and OH. Consequently, Ru@TiO_2 not only surpasses commercial PtRu/C in alkaline HOR activity but also demonstrates unprecedented CO tolerance. Even under 1000 ppm CO, its HOR activity decreases by less than 8%; remarkably, in an atmosphere containing 10 vol.% CO, Ru@TiO_2 continues to selectively catalyze HOR, whereas PtRu/C and Pt/C catalysts are completely deactivated. Building upon Zhou's work, Jin et al. constructed Ru/TiO_2 heterostructures via a "pre-oxidation

Table 1 Summary of the performances of composite catalysts for alkaline HOR

Catalyst	Electrolyte	Catalyst loading ($\mu g_{PGM} \cdot cm_{geo}^{-2}$)	Exchange current density ($mA \cdot cm_{PGM}^{-2}$)	Mass activity ($A \cdot mg_{PGM}^{-1}$)	References
IO-Ru-TiO_2/C	0.1 M KOH	25.48	0.108	0.907@50 mV	[83]
Ru@TiO_2	0.1 M KOH	25	—	0.282@20 mV	[53]
Ru/TiO_2	0.1 M KOH	200_{cat}[a]	0.921	1.529@50 mV	[84]
Ru_{SA}-Ru_{NC}/TiO_{2-x}	0.1 M KOH	200_{cat}[a]	4.2	—	[85]
Ru/TiN-TiO_2	0.1 M KOH	11.3	0.61	1.956@50 mV	[86]
Ru-SA-ZrO_{2-x}/C	0.1 M KOH	1.25	—	6.79@50 mV	[87]
PtNb/NbO_x-C	0.1 M KOH	20	0.8	0.360@25 mV	[88]
Ru/VOC	0.1 M KOH	18.47	0.12	3.44@25 mV	[89]
Ru-$Cr_1(OH)_x$	0.1 M KOH	60	0.28	—	[90]
Ru-CrO_x@CN	0.1 M KOH	—	1.04	13.76@20 mV	[55]
Ir/O-MoO_2	0.1 M KOH	25	1.96	—	[91]
PtMo/MoO_{x-1}/C	0.1 M KOH	9.43	0.83	3.19@50 mV	[92]
Pt/MoO_3-CN_x	0.1 M KOH	5.06	1.198	0.49@400 mV	[93]
IrWO_x/C	0.1 M KOH	2.01	1.56	2.16@50 mV	[94]
Ru-WO_3	0.1 M KOH	—	—	—	[95]
Ru/$WO_{2.9}$/C	0.1 M KOH	10	1.32	8.29@50 mV	[96]
Ru-WO_x/NC	0.1 M KOH	9.7	0.98	6.44@30 mV	[97]
Pd/MnO_2	0.1 M KOH	—	—	—	[98]
Ru-MnO/C	0.1 M KOH	20	2.58	0.78@50 mV	[99]
$Mn_1O_x(OH)_y$@Ru/C	0.1 M KOH	28	0.125	—	[100]
Pd-RuO_2/C	0.1 M KOH	~ 40	0.049	—	[101]
Pt-RuO_2/C	0.1 M NaOH	—	—	—	[102]
Ru/RuO_2	0.1 M KOH	20	—	~ 0.02@50 mV	[103]
Ru/SnO_2	0.1 M KOH	—	—	—	[104]
Pd/C-CeO_2	0.1 M KOH	—	54.5	—	[105]
Pd-CeO_2/C	0.1 M NaOH	2.8	—	—	[106]
Ru/CeO_2	0.1 M KOH	303_{cat}[a]	0.07	—	[107]
Ru/CeO_2(v)/C	0.1 M KOH	10	2.85	8.06@50 mV	[108]
Ir/MoS_2	0.1 M KOH	200_{cat}[a]	1.28	—	[109]
PtRu/Mo_2C-TaC	0.1 M KOH	13	0.291	0.403@25 mV	[110]
Ir_{SA}-Mo_2C/C	0.1 M KOH	3.2	4.1	17.9@50 mV	[111]
$Pt_{SA}Mo_2C$-NC	0.1 M KOH	—	—	2.15@50 mV	[112]
Ru-WC_x	0.1 M KOH	1.17	1.44	7.844@50 mV	[113]
Ru SA/WC_{1-x}	0.1 M KOH	—	—	0.876@50 mV	[114]
Ru-Ru_2P/C	0.1 M KOH	8.33	—	1.265@50 mV	[115]
Pt_{nc}/MoN	0.1 M KOH	3.93	1.927	0.866@50 mV	[116]
$Pt_{0.25}Ru_{0.75}$/pN-C	0.1 M KOH	2.3	2.12	—	[117]
$(RuCo)_{NC+SAs}$/N-CNT	0.1 M KOH	7	2.62	7.35@50 mV	[12]
Pd_{SA}/N, S-OPC	0.1 M KOH	250_{cat}		27.71@50 mV	[118]
RuSA/NSG	0.1 M KOH	—	—	—	[119]
RuNi/NC	0.1 M KOH	500_{cat}[a]	—	0.13@50 mV	[120]
Pt_1@Co_1-CN	0.1 M KOH	11.2	—	0.68@50 mV	[121]
s-Ru_1Pt@W_1/NC	0.1 M KOH	306_{cat}[a]	0.14	7.54@50 mV	[122]
Ru_1Pt_n-SAA	0.1 M KOH	—	1.992	4.71@50 mV	[123]
$RuNi_1$ NCs	0.1 M KOH	8.8	—	2.7@50 mV	[124]
Mo-Pt/NC	0.1 M KOH	10	—	4.549@50 mV	[125]
Ce_1Ru/C	0.1 M KOH	5.2	—	40.81@50 mV	[126]
La_1Pt@HCS	0.1 M KOH	10	1.55	2.42@25 mV	[127]

[a] $_{cat}$ refers to catalyst loading when the noble metal loading was not reported.

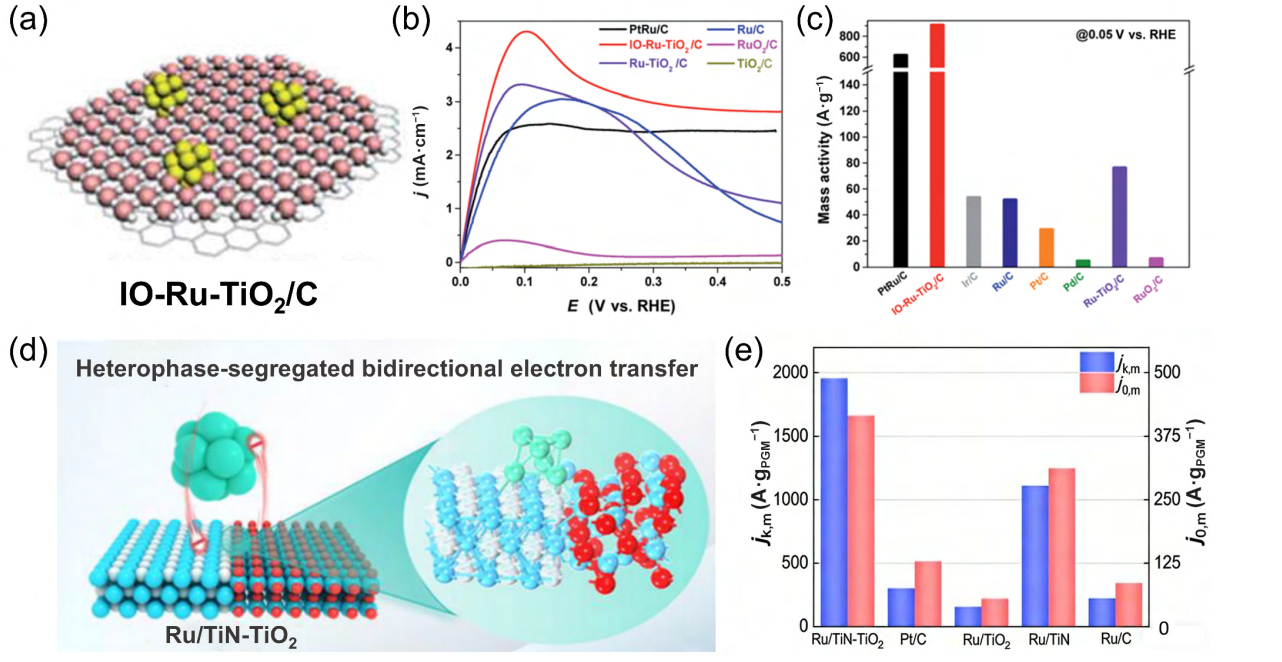

Figure 8 (a) Schematic illustration of IO-Ru-TiO_2/C architecture. (b) HOR polarization curves of PtRu/C, IO-Ru-TiO_2/C, Ru-TiO_2/C, Ru/C, RuO_2/C, and TiO_2/C. (c) Corresponding mass activities of the catalysts in (b) and other reference catalysts at 0.05 V vs. RHE. Reproduced with permission from Ref. [83], © The Royal Society of Chemistry 2020. (d) Proposed mechanism of bidirectional electron transfer at the Ru/TiN-TiO_2 interface. (e) Mass-normalized kinetic current density ($j_{k,m}$, at 50 mV vs. RHE) and exchange current density ($j_{0,m}$) of Ru/TiN-TiO_2 and benchmark catalysts. Reproduced with permission from Ref. [86], © Wiley-VCH GmbH 2025.

and subsequent reduction" strategy, further confirming the generality of electron transfer from TiO_2 to Ru [84]. In parallel, Cong et al. developed TiO_{2-x} supports hosting both Ru single atoms and clusters (Ru_{SA}-Ru_{NC}/TiO_{2-x}) [85]. Under strong Ru–Ti bonding, significant electron injection was achieved, which not only boosted HOR activity but also provided outstanding stability: Oxygen vacancies promoted the *in situ* formation of Ti^{3+} species that preferentially oxidized, thereby protecting Ru sites at high potentials (up to 1.2 V). This design delivered exceptional resistance to oxidation and CO poisoning.

Recently, Li et al. introduced titanium nitride (TiN_x) as a secondary support into the Ru-TiO_2 system, constructing a Ru/TiN_x-TiO_2 composite catalyst [86]. Using a "TiO_2 nanorod ammonolysis-*in situ* Ru deposition" strategy, they established a well-defined heterointerface within the composite support. The core innovation lies in the proposed bidirectional electron relay mechanism, which synergistically addresses both Ru oxidation and competitive adsorption of intermediates at high potentials through dynamic electron flow and spatial site separation. On one hand, during the initial reaction stage, Ru donates electrons to the high-work-function TiN_x, shifting its d-band center downward and weakening H adsorption to prevent H_{ad} accumulation. On the other hand, under high potential conditions, TiO_2 supplies electrons back to Ru via Ru–Ti–O bonds, effectively mitigating electron loss and surface oxidation of Ru (Fig. 8(d)). Meanwhile, Ti(N)–Ru bridge sites and Ru-top sites selectively adsorb OH and H, respectively, enabling spatial separation of key intermediates and significantly accelerating the Volmer step. The catalyst exhibits outstanding alkaline HOR performance, delivering a mass activity of 1.956 A·mg_{Ru}^{-1} at 50 mV overpotential and maintaining full activity at 1.1 V, markedly outperforming Pt/C benchmarks, pushing the performance of TiO_2-based composite catalysts to a new level (Fig. 8(e)). Following systematic investigations on TiO_2 as a composite component for tuning the electronic structure and performance of Ru-based HOR catalysts, ZrO_2—another IVB-group transition metal oxide with similar chemical properties—has emerged as an important component for constructing high-performance Ru catalysts, further expanding the design strategies and performance boundaries of this material class. Zhang et al. reported a Ru single-atom catalyst anchored on oxygen-vacancy-rich ZrO_{2-x}/C (Ru-SA-ZrO_{2-x}/C) [87]. Its outstanding alkaline HOR performance originates from the synergistic effects of electronic interactions at the Ru-ZrO_{2-x} interface and abundant oxygen vacancies: Electron transfer from ZrO_{2-x} to Ru not only significantly weakens the HBE to prevent excessive H_{ad} accumulation, but also lowers the OH adsorption energy, suppressing Ru site oxidation at high potentials. Meanwhile, the plentiful oxygen vacancies facilitate OH^- transport at the interface, collectively optimizing the Volmer step. This electronic structure also induces weaker CO adsorption and faster CO oxidation/removal, enhancing the catalyst's resistance to CO poisoning. As a result, the catalyst achieves a mass activity of 6.789 A·mg_{Ru}^{-1} at 50 mV overpotential, ranking among the top reported alkaline HOR catalysts; it retains 81.2% of the current density after 18,000 s of continuous operation and maintains 81.9% of its initial activity in 1000 ppm CO/H_2, demonstrating outstanding application potential.

4.1.2 *VB-group transition metal oxides (VO_x and NbO_x)*

Building on the research of IVB-group metal oxide composite catalysts, attention has been extended to VB-group transition metal oxides, such as NbO_x and VO_x. In earlier work, Ghoshal et al. developed a PtNb/NbO_x-C composite electrocatalyst, where Nb species coexisted in two forms: a PtNb alloy phase and a NbO_x oxide phase [88]. The PtNb alloy weakened the Pt–H bond via electronic effects, facilitating H_{ad} desorption, while NbO_x, with its strong oxophilicity, adsorbed and supplied active OH_{ad} species. The

synergy between these two components significantly accelerated the Volmer step, demonstrating the potential of VB-group metal oxides to modulate the adsorption behavior of reaction intermediates.

Based on this, Wang et al. successfully constructed a Ru catalyst doped with atomically dispersed V–O species on a carbon support (Ru/VOC) via a metal–organic framework precursor combined with an acid-etching strategy [89]. This system further expanded the functional scope of VB-group oxides in electrocatalysis, exhibiting a refined synergistic mechanism of "spatial partitioning and electronic effect": The atomically dispersed V–O species acted as highly efficient OH adsorption sites, mitigating OH poisoning at Ru active sites and allowing Ru to focus on H adsorption and conversion; simultaneously, electron transfer from Ru to the V–O/carbon support shifted the d-band center of Ru downward, optimizing H adsorption energy and enhancing CO tolerance. Consequently, Ru/VOC displayed excellent catalytic activity and CO tolerance in alkaline HOR, providing a new strategy for designing high-performance, stable anode catalysts for AEMFCs.

4.1.3 *VIB-group transition metal oxides (CrO_x, MoO_x, and WO_x)*

Compared with Group VB, transition metal oxides of Group VIB (including oxides of Cr, Mo, and W) exhibit more versatile regulatory mechanisms and functionalities in electrocatalytic HOR, attracting increasing research attention in recent years. In the study of CrO_x, the work of Zhang et al. laid a foundation for understanding their functional mechanisms [90]. They successfully synthesized catalysts in which atomically dispersed $Cr_1(OH)_x$ clusters modified Ru nanoparticles. The key feature of this structure is that the isolated Cr^{3+} centers form a unique coordination environment rich in active oxygen species. Without altering Ru metal characteristics, these centers reconstruct the reaction interface and pathways through a "triple action" mechanism: (i) providing highly active oxygen species to synergistically regulate the adsorption energies of H and OH, preventing H poisoning on Ru surfaces while ensuring OH availability; (ii) facilitating hydrogen spillover and lowering intermediate diffusion barriers; and (iii) directly participating in water formation through oxygen in $Cr_1(OH)_x$, significantly reducing the energy barrier of the Volmer step. Extending this strategy, Zhang et al. further developed a Janus-type heterostructure in which crystalline Ru clusters are tightly coupled with amorphous CrO_x clusters (Figs. 9(a) and 9(b)) [55]. The strong cluster–cluster coupling induces pronounced interfacial electronic interpenetration, driving electron transfer from Ru to CrO_x and achieving a deeper-level reconstruction of the interfacial electronic structure. As a result, Ru and CrO_x clusters are respectively optimized for H desorption and OH adsorption. Benefiting from this bifunctional synergistic mechanism, the catalyst exhibits a mass activity of 13.76 $A{\cdot}mg_{Ru}^{-1}$ at 20 mV in alkaline HOR (Fig. 9(c)), demonstrates excellent CO tolerance, and maintains uninterrupted operation in AEMFCs for 105 h without degradation. Its performance far surpasses that of conventional Pt/C and Ru/C catalysts, providing a new paradigm for designing efficient non-platinum electrocatalysts (Fig. 9(d)).

MoO_x, as another important class of VIB-group materials, also exhibits excellent regulatory mechanisms in alkaline HOR. Li et al. were among the first to reveal the decisive role of interfacial bonding type from an electronic structure perspective [91]. By precisely controlling the annealing atmosphere of MoO_2 supports, they successfully constructed Ir/MoO_2 catalysts featuring two distinct interfacial chemical bonds: Ir–O and Ir–Mo. The Ir–O–Mo bonds induce localized electron transfer, effectively lowering the d-band center of Ir, optimizing hydrogen adsorption free energy, and enhancing resistance to hydroxyl poisoning. In contrast, interfaces dominated by Ir–Mo metallic bonds lead to an upward shift of the

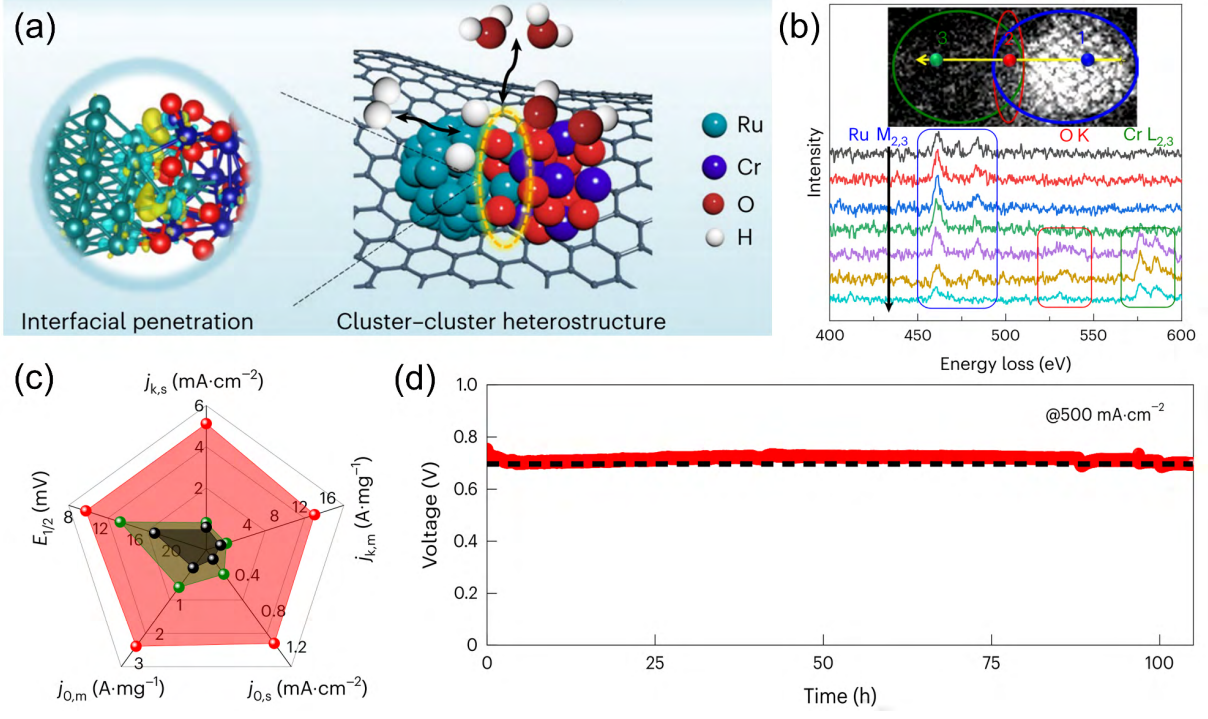

Figure 9 (a) Schematic illustration of the cluster–cluster heterostructured catalyst. (b) The line scanning electron energy loss spectroscopy (EELS) spectra on one Ru-CrO_x cluster. Insert is the scanning path in the STEM-HAADF image for EELS profile spectra extraction. (c) Comparisons of $E_{1/2}$, mass- and ECSA-normalized activities of Ru–CrO_x@CN (red), Ru@CN (green), and Pt/C (black). (d) Long-term stability tests of the H_2–O_2 fuel cell at 500 $mA{\cdot}cm^{-2}$ using the Ru–CrO_x@CN (0.055 $mg_{Ru}{\cdot}cm^{-2}$) as the anode catalyst. Reproduced with permission from Ref. [55], © Zhang, B. X. et al. 2024.

d-band center, with limited performance improvement. As a result, Ir/O-MoO_2 exhibited a mass activity of 1.96 $mA{\cdot}cm_{ECSA}^{-2}$, significantly higher than that of Ir/Mo-MoO_2, and approximately 3.7 times higher than conventional Ir/C catalysts. This study clearly demonstrated that the essence of interfacial chemical bonding is the core factor in tuning the electronic structure. Extending this approach, Luo et al. designed an interfacial electrocatalyst composed of PtMo alloy nanoparticles and amorphous MoO_x atomic layers on the surface (PtMo/MoO_x) [92]. Through interfacial synergistic effects, they achieved precise tuning of H, OH, and CO adsorption behaviors, obtaining moderately weakened H adsorption and enhanced OH adsorption, which resulted in high HOR activity and effectively mitigated CO poisoning. Moreover, Samanta et al. focused on the mass transport functionality of MoO_x, providing a complementary mechanism to the above electronic effects [93]. In the Pt/MoO_3 system, MoO_3 not only modulates the electronic structure but also forms heterointerfaces with Pt that act as efficient "hydrogen spillover" channels, facilitating the migration and desorption of adsorbed H from Pt sites to the MoO_3 surface, thereby directly optimizing the adsorption–desorption kinetics during the HOR process.

Following the expansion of VIB oxide design concepts through CrO_x at the atomic interfacial level and MoO_x via combined electronic-mass transport functionality, research on WO_x has further integrated and innovated these mechanisms, highlighting the exceptional functional versatility of this class of materials. Early studies focused on the electronic modulation effect of WO_x. Fu et al. reported that in Ir/WO_x systems, the OH species adsorbed on WO_x do not directly participate in the reaction, rather optimize the electronic structure of Ir sites through interfacial electronic interactions, lowering the HBE and enhancing the intrinsic HOR kinetics [94]. With further investigation, the classical bifunctional role of WO_x became evident. Studies by Liu et al. [95] and Cheng et al. [96] demonstrated that in Ru/WO_x systems, WO_x not only provides OH adsorption sites but also modulates Ru–H interactions via interfacial electronic transfer, achieving synergistic optimization of H and OH adsorption energies and delivering catalytic performance far exceeding that of commercial Pt/C. Most notably, Zheng et al. went beyond traditional adsorption-based design paradigms. Inspired by the "spillover" phenomenon observed in Cr/Mo systems, they discovered a more complex functional evolution in WO_x [97]: The oxygen vacancies and non-stoichiometric nature of WO_x act as a "proton sponge", efficiently accepting and consuming H_{ad} species spilled from Ru sites and rapidly reacting with interfacial OH_{ad} to form water. This mechanism fully circumvents the competitive adsorption of H_{ad} and OH_{ad} on a single site, ultimately enabling an AEMFC peak power density of 1.36 $W{\cdot}cm^{-2}$ at an ultralow Ru loading (0.05 $mg{\cdot}cm^{-2}$) and maintaining stable operation for 80 h.

4.1.4 *VIIB-group transition metal oxides (MnO_x)*

Following systematic investigations of the multiple regulatory mechanisms of VIB transition metal oxides (Cr, Mo, and W), MnO_x from the VIIB group has emerged as another important modifying component, demonstrating a remarkable evolution in HOR catalyst design from passive support to active functional center. Early studies, such as the Pd/MnO_2 catalyst prepared by Cruz-Reyes et al., indicated that MnO_2 nanorods primarily served as a physical support, effectively preventing the aggregation of Pd nanoparticles (~ 11 nm), highlighting the fundamental role of the support in providing dispersion and stabilizing active sites [98]. With further research, the intimate electronic interactions between MnO_x and metal active sites, as well as their ability to regulate reaction pathways, have become increasingly evident. Zhang et al. constructed strongly coupled Ru–O–Mn interfaces in Ru-MnO/C heterocluster structures, inducing electron transfer simultaneously from Ru to O and from Mn to O [99]. This electronic reconstruction effectively lowered the d-band center and modulated the adsorption properties of Ru, simultaneously weakening its adsorption of H, OH, and CO intermediates. As a result, the Ru-MnO/C catalyst achieved a high activity of 2.58 $mA{\cdot}cm_{Ru}^{-2}$ and exhibited only 17.4% activity loss under 1000 ppm CO, demonstrating the high activity and anti-poisoning capability imparted by electronic-level synergy. Notably, MnO_x exhibits a unique function in addressing the challenge of high-potential deactivation of anode catalysts. Shi et al. designed $Mn_1O_x(OH)_y$@Ru/C catalysts (Fig. 10(a)), where atomically dispersed $Mn_1O_x(OH)_y$ clusters enabled dynamic potential-dependent regulation of the electronic structure of Ru nanoparticles [100]. At high potentials (> 0.1 V vs. RHE), interfacial charge transfer induced a spin-state transition in Mn ($Mn^{3+} \rightarrow Mn^{2+}$) (Fig. 10(b)), reducing the electron density at Ru sites and effectively suppressing excessive adsorption of oxygen species on the Ru surface (Fig. 10(c)). Consequently, the catalyst maintained high activity and stability across a wide potential window (0–1.0 V) and drove an AEMFC to achieve a peak power density of 1.731 $W{\cdot}cm^{-2}$ (Figs. 10(d) and 10(e)).

4.1.5 *Other tetravalent metal oxides (MO_2, M = Ru, Sn, and Ce)*

After extensively investigating the regulatory mechanisms of IVB–VIIB metal oxides, attention has been further extended to other metal oxides with tetravalent characteristics, such as CeO_2, SnO_2, and RuO_2. Pagliaro et al. systematically compared the enhancing effects of various MO_x (M = Zr, Ce, Sn, and Ru) on Pd, demonstrating that all could promote HOR through a classical bifunctional mechanism: Pd sites facilitated H adsorption and dissociation, while the oxides provided OH adsorption sites [101]. Among them, RuO_2 exhibited the highest alkaline HOR activity due to its strongest oxyphilicity. Similarly, Wang et al. [102] and Zhang et al. [103] investigated Pt/RuO_2 and Ru (100)/RuO_2 (200) composite catalysts, further confirming that metal-oxide hybrids can enhance HOR kinetics by optimizing H and OH adsorption via the classical bifunctional pathway. Notably, in the latter study, significant interfacial electronic interactions were observed due to the specific crystal facets, enabling the Ru (100)/RuO_2 (200) catalyst to achieve a high exchange current density of 8.86 $mA{\cdot}cm^{-2}$ under alkaline conditions, with only a 10% activity loss after 8 h at 0.1 V (vs. RHE), demonstrating excellent catalytic activity and durability. Going beyond the conventional bifunctional mechanism, Yang et al. introduced an innovative "hydrogen intercalation pool" concept in the Ru/SnO_2 system [104]. By pre-intercalating hydrogen (H_i) into the SnO_2 lattice interstices, the catalyst dynamically eliminated interface OH_{ad} poisons: At high potentials, H_i migrated to the interface and reacted with OH_{ad} to form water ($H_i + OH_{ad} \rightarrow H_2O$), while at low potentials, H_{ad} could overflow back into SnO_2 and regenerate H_i, completing a dynamic cycle. This mechanism enabled the catalyst to maintain 87.7% of its activity even at high potentials (1.0 V vs. RHE), significantly alleviating high-potential deactivation of anode catalysts. Among various tetravalent metal oxides, CeO_2 has attracted the most extensive and in-depth

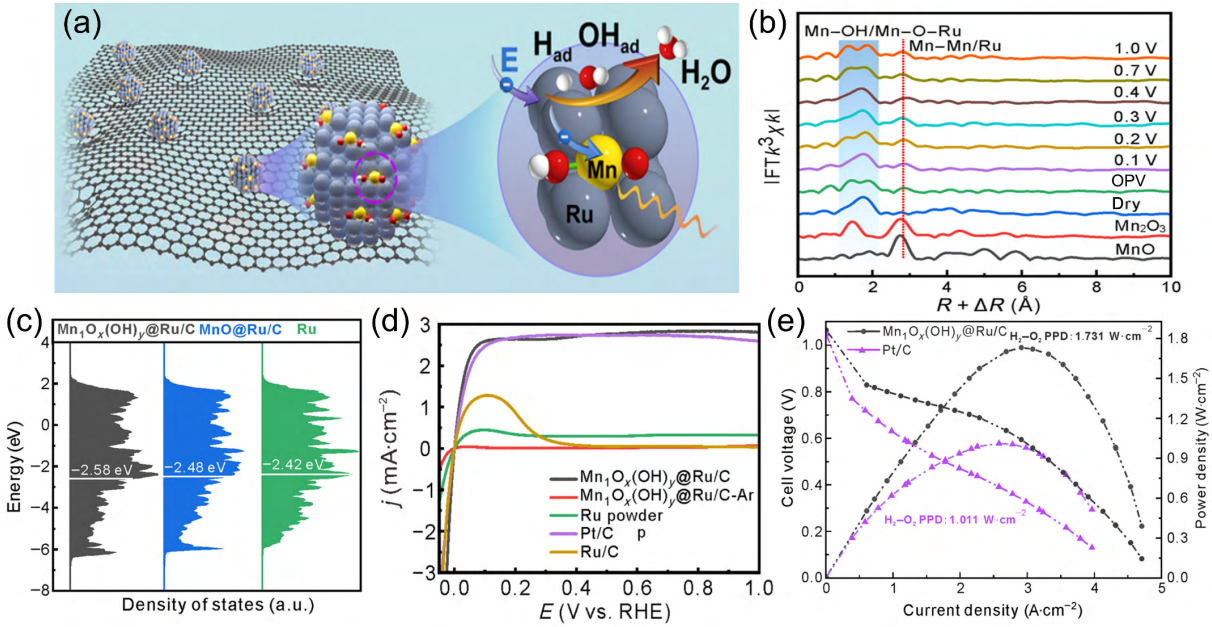

Figure 10 (a) Proposed mechanism of $Mn_1O_x(OH)_y$@Ru/C for the alkaline HOR. (b) Fourier transform (FT) k^3-weighted χ(k) function of the extended XAFS (EXAFS) spectra for the Mn K-edge of $Mn_1O_x(OH)_y$@Ru/C at different overvoltages. (c) The d-band centers of Ru in the three catalysts. (d) Polarization curves of $Mn_1O_x(OH)_y$@Ru/C, Pt/C, Ru/C, and Ru powder catalysts in H_2-saturated and Ar-saturated 0.1 M KOH solutions at a scan rate of 1 mV·s^{-1} and a rotation speed of 1600 rpm. (e) Polarization and power density curves of H_2/O_2 AEMFCs with $Mn_1O_x(OH)_y$@Ru/C, and Pt/C in the cathode. Reproduced with permission from Ref. [100], © American Chemical Society 2024.

investigation due to its excellent oxygen storage-release capability and tunable O_v concentration. Its role has gradually evolved from early interface electronic effects to active site design dominated by oxygen vacancies. Miller et al. first revealed the electronic effect at the Pd/CeO_2 interface: CeO_2 acts as an electron acceptor, lowering the electron density of Pd to weaken Pd–H adsorption while simultaneously providing OH_{ad}, together enhancing the exchange current density to 54.5 mA·cm$_{Pd}^{-2}$, more than 20 times that of Pd/C [105]. By precisely controlling the interfacial contact between Pd and CeO_2, Yu et al. demonstrated that effective electron transfer and optimization of the Volmer step occur only when the two phases achieve small particle size, uniform dispersion, and strong interfacial interaction [106]. In recent years, research has focused on precisely tuning the interfacial electronic structure and reaction pathways via CeO_2 oxygen vacancies. Wang et al. prepared Ru/CeO_2 catalysts using CeO_2 nanorods rich in oxygen vacancies, significantly enhancing both alkaline HOR activity and CO tolerance [107]. Cheng et al. represent the latest advance in this direction: Ru catalysts supported on oxygen-vacancy-rich CeO_2(v) were synthesized via a metal–organic framework (MOF)-templated method [108]. Compared with pristine CeO_2, Ru/CeO_2(v)/C exhibits a sharp and symmetric signal at g = 2.003. The electrophilic nature of CeO_2(v) induces electron transfer from Ru, which weakens the HBE while the oxygen vacancies act as efficient OH adsorption sites, enabling synergistic adsorption and spatial separation of H_{ad} and OH_{ad}, thus significantly promoting Volmer kinetics. This catalyst achieves a mass activity of 8.06 A·mg$_{Ru}^{-1}$ at 50 mV and a specific activity of 2.85 mA·cm^{-2}, corresponding to 19.6 and 20.1 times enhancements over commercial Pt/C, and demonstrates excellent stability and CO tolerance.

In summary, metal oxides have been composited with metal nanoparticles to form HOR composite catalysts, since the metal oxides have good stability in alkaline conditions. IVB, VB, VIB, and VIIB transition-metal oxides, along with other tetravalent oxides, have emerged as versatile components in composite catalysts for alkaline HOR. Despite their differences in elemental composition, crystal structure, and interfacial properties, they share common mechanisms—such as interfacial electronic reconstruction and oxygen-vacancy engineering—that markedly optimize the adsorption of key intermediates (H, OH, and CO) on noble-metal active sites, thereby enhancing HOR activity, high-potential stability, and CO tolerance. The stronger hydrophilicity of the metal oxides than metal also manipulates the interfacial water structures. IVB oxides (e.g., TiO_2 and ZrO_2) are distinguished by their strong electronic modulation and structural adaptability, effectively mitigating the oxidative instability and poor CO resistance of Ru; VB oxides (e.g., NbO_x and VO_x) primarily enhance HOR activity and stability via bifunctional pathways; VIB oxides (e.g., CrO_x, MoO_x, and WO_x) exhibit synergistic advantages spanning atomically dispersed structures, coupled electronic-mass transport regulation, and "proton-sponge"-mediated hydrogen spillover channels; and VIIB oxides (e.g., MnO_x) have evolved from passive supports to dynamic potential-responsive functional centers; and other tetravalent oxides (e.g., RuO_2, SnO_2, and CeO_2) enrich hydrogen management and pathway modulation through strategies, such as bifunctional catalysis, hydrogen-intercalation pools, and vacancy engineering. Although differing in their regulatory mechanisms and functional emphases, all these oxides, through carefully engineered composite interfaces, help overcome the intrinsic challenges of single-metal or alloy catalysts in alkaline HOR—including sluggish kinetics, susceptibility to oxidative deactivation, and competitive adsorption of intermediates—thus offering a robust and diverse materials platform for the design of high-performance, low-noble-metal-loading anode catalysts in AEMFCs.

4.2 Non-oxide components

After systematically examining metal oxides and their multivariate regulation mechanisms, the research scope has further expanded to

another important class of non-oxide materials—namely sulfides, carbides, phosphides, and nitrides. Owing to their metal-like conductivity, tunable electronic structures, and unique surface chemistry, these compounds exhibit multiple promotion pathways in alkaline HOR catalysis, ranging from HBE optimization and bifunctional catalysis to novel interfacial water-mediated mechanisms, providing new material platforms and theoretical frameworks for catalyst design.

In the relatively less explored field of sulfide-based catalysts, Liu et al. conducted a pioneering study in which ultrasmall Ir nanoclusters (< 2 nm) were epitaxially grown on the MoS_2 surface (Fig. 11(a)) [109]. This configuration induced interfacial electron transfer from MoS_2 to Ir (Figs. 11(b) and 11(c)), creating electron-rich Ir sites that effectively lowered its d-band center and optimized the HBE, resulting in significantly enhancing the alkaline HOR kinetics. Similarly, Hamo et al., following an HBE-regulation strategy, deposited PtRu nanoparticles onto a Mo_2C-TaC composite support. Benefiting from the high proportion of cubic-phase Mo_2C (65.57%) and strong metal–support interactions, the HBE was optimized to −0.167 eV, which delivered excellent activity and stability, with the current density at 25 mV being 1.65 and 1.50 times higher than those of the single Mo_2C and Mo_2C-W_2C supports, respectively [110].

However, sole HBE regulation has its limitations, and subsequent studies have gradually revealed the greater potential of bifunctional catalytic mechanisms in carbides. Fang et al. precisely substituted Mo sites in the Mo_2C lattice with Ir atoms to construct an Ir single-atom catalyst (Ir_{SA}-Mo_2C/C) [111]. By leveraging the synergistic interaction between Ir and neighboring Mo sites, the H and OH adsorption free energies were simultaneously optimized, lowering the water formation barrier to 0.20 eV and achieving a mass activity of 17.9 $A{\cdot}mg_{Ir}^{-1}$ at ultralow Ir loading with negligible decay over 30,000 cycles. Yang et al. designed a yolk–shell structure with Mo_2C as the core and N-doped carbon as the shell, anchoring Pt single atoms (Pt-SAs) at Mo_2C surface defects. This induced electronic transfer from Pt to Mo_2C, synchronously optimizing H and OH adsorption while enhancing CO tolerance through the strong adsorption of the Mo_2C core [112]. Similarly, Wang et al. stabilized nearly zero-valent Ru single atoms on WC_x supports, forming metal–metal interactions between Ru and W sites, achieving dual-site cooperation to optimize H and OH adsorption separately, with a mass activity of 7.844 $A{\cdot}mg_{Ru}^{-1}$ [113]. Additionally, Su et al. explored phosphide-based catalysts, developing a Ru-Ru_2P/C heterostructure that revealed non-monotonic HOR activity across the full pH range and clarified the roles of H, H_2O, and OH intermediates, ultimately identifying OH adsorption energy as the key factor under alkaline conditions and achieving activity surpassing that in acid [115].

Beyond conventional HBE and classical bifunctional mechanisms, recent studies have begun to uncover more innovative catalytic pathways. Notably, Jin et al. investigated Pt nanocluster/MoN (Pt_{nc}/MoN) systems and revealed a novel mechanism of interfacial water microenvironment reconstruction [116]. Their study showed that Pt_{nc}/MoN not only optimizes the d-band center of Pt via strong electronic metal–support interactions to achieve near-thermoneutral HBE (Fig. 11(d)), but also enhances OHBE to induce coordination between adsorbed OH_{ad} and alkali metal cations (K^+) in the double layer. This coordination alleviates the cation-induced exclusion of interfacial water molecules and reconstructs a continuous hydrogen-bond network within the "gap region" (Fig. 11(e)). This synergistic mechanism enables Pt_{nc}/MoN to exhibit an exceptionally high intrinsic activity of 1.92 $mA{\cdot}cm^{-2}$ for alkaline HOR, outperforming Pt NPs/MoN (Pt_{np}/MoN) and commercial Pt/C (Fig. 11(f)), breaking the traditional limitation of catalyst design that focuses solely on thermodynamic adsorption optimization, and providing a new paradigm for designing highly

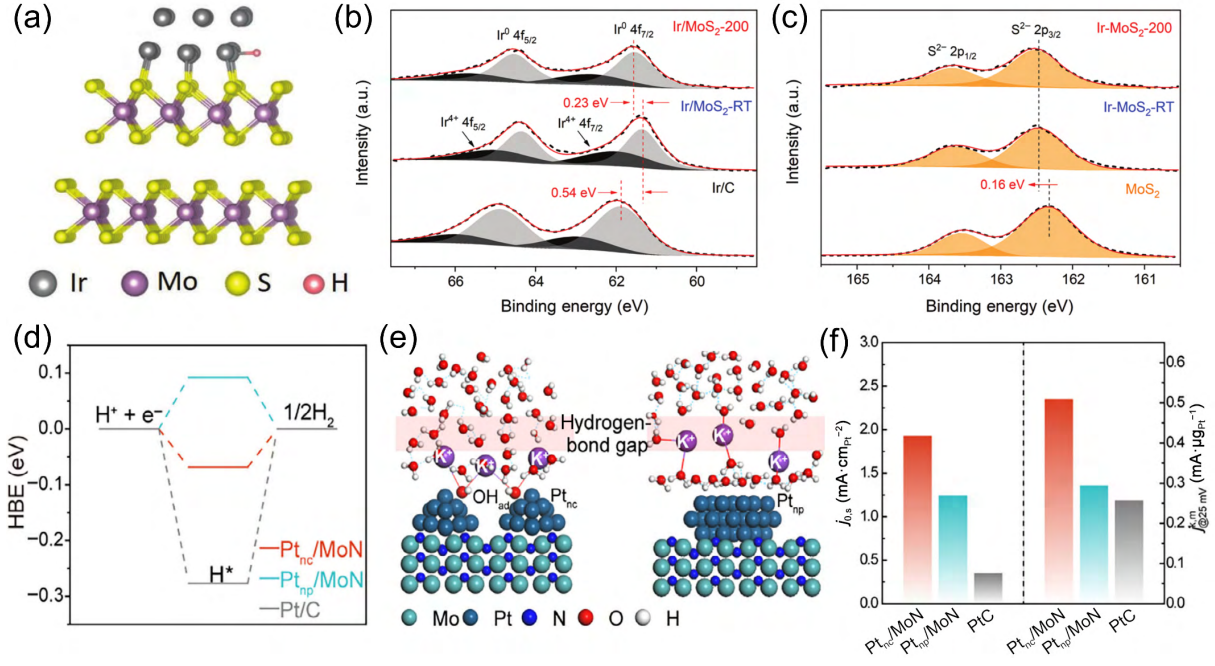

Figure 11 (a) Structure model of Ir/MoS_2-200 used for the DFT calculation. XPS spectra of (b) Ir 4f in synthesized Ir/C, Ir/MoS_2-RT, and Ir/MoS_2-200 samples and (c) S 2p in MoS_2, Ir/MoS_2-RT, and Ir/MoS_2-200 samples. Reproduced with permission from Ref. [109], © Wiley-VCH GmbH 2022. (d) Free energy diagram of adsorbed hydrogen of Pt d-orbitals for Pt_{nc}/MoN, Pt_{np}/MoN, and Pt/C. (e) Schematic illustration of interfacial water structures of Pt_{nc}/MoN and Pt_{np}/MoN. (f) Comparison of the $j_{0,s}$ and $j_{k,m}$ of Pt_{nc}/MoN, Pt_{np}/MoN, and Pt/C. Reproduced with permission from Ref. [116], © Wiley-VCH GmbH 2025.

efficient electrocatalysts via interfacial microenvironment engineering.

In summary, non-oxide components have emerged as increasingly important players in HOR electrocatalysis. Their functional mechanisms have evolved markedly, progressing from early-stage single-parameter HBE regulation to mature bifunctional catalysis and, more recently, to advanced management of the interfacial water microenvironment. These materials not only enrich the family of composite catalysts but also open new avenues for the rational design of high-performance and highly stable AEMFCs anode catalysts by providing unique interfacial properties and mechanistic insights. Although oxides and non-oxides differ in composition and structure, both aim to precisely tailor interfacial electronic and structural properties to address core challenges in alkaline HOR, including sluggish kinetics and limited stability. Overall, the compositional and functional diversity of composite materials has positioned them as a central pillar in current alkaline HOR electrocatalyst research, providing a rich materials platform and design strategies to reduce noble metal dependence and enhance AEMFCs performance. However, the stability of the non-oxide components at evaluated potential might be an issue that limits their applications. For example, sulfides tend to be oxidized to sulfonates. The microenvironmental control to stabilize the non-oxide components under AEMFC working conditions is therefore important.

4.3 Single-atom catalysts

In parallel with efforts to rationally design composite electrocatalysts through elemental hybridization and interfacial engineering at the nanoscale, the pursuit of ultimate atomic utilization efficiency and precise regulation of active sites has driven the rapid emergence of SACs across a broad range of catalytic fields, including electrosynthesis [128–130], energy storage [131–134], and fuel cell technologies [135–137]. Characterized by atomically dispersed metal centers, SACs not only achieve the theoretical limit of metal utilization but also provide an ideal platform for establishing clear structure–activity relationships at the atomic scale [138, 139]. For the alkaline HOR, the design philosophy of SACs goes beyond conventional composite strategies and instead focuses on the fine modulation of the coordination environment of individual metal atoms, enabling unprecedented precision in optimizing the adsorption behavior of key intermediates (H, OH, and water) [37, 140]. It is well recognized that the controllable synthesis and stable existence of single atoms fundamentally rely on their interaction with the support [141, 142]. The support is not only essential for anchoring and stabilizing isolated metal atoms, but also plays a decisive role in determining the ultimate catalytic performance. Accordingly, based on the intrinsic characteristics of the supports, alkaline HOR single-atom catalysts can be broadly classified into three main categories: carbon-supported single-atom catalysts, single-atom alloys, and transition metal compound-supported single-atom catalysts. In the following, recent advances in each category will be systematically reviewed, with emphasis on how support design and atomic-scale structural engineering address the key challenges of activity, stability, and cost in alkaline HOR electrocatalysts.

4.3.1 Carbon-supported single-atom catalysts

As one of the earliest and most widely adopted supports for stabilizing single-atom active sites, carbon-based materials have long occupied a central position in single-atom catalyst design owing to their high structural tunability and excellent electrical conductivity. Ni et al. employed a porous nitrogen-doped carbon (pN-C) derived from a covalent organic framework as the support, where the interconnected macro-mesoporous architecture enabled uniform catalyst dispersion [117]. By anchoring Pt single atoms via nitrogen coordination, they successfully constructed a composite catalyst consisting of PtRu nanoparticles with an average size below 1.6 nm and atomically dispersed Pt-SAs. In this system, Ru modulates the electronic structure of Pt to reduce the hydrogen binding energy, while the pN-C-anchored Pt-SAs promote the formation of strongly hydrogen-bonded, oxygen-down interfacial water. These two effects synergistically overcome the kinetic limitations of the alkaline HOR through complementary regulation of the electronic structure and the interfacial water configuration. When implemented in a fuel cell, the catalyst delivered outstanding performance at a low platinum-group metal loading of 0.16 $mg_{PGM}·cm^{-2}$, achieving a peak power density of 1.46 $W·cm^{-2}$, a current density of 1.5 $A·cm^{-2}$ at 0.65 V, and a PGM utilization as high as 10.82 $W·mg_{PGM}^{-1}$. Moreover, only marginal performance decay was observed after 100 h of operation, underscoring the advantages of this catalyst in terms of high activity, excellent stability, and reduced noble-metal usage.

Along similar lines, Cui et al. sought to enhance alkaline HOR performance through multimetallic synergy and structural integration. They developed a composite catalyst anchored on nitrogen-doped carbon nanotubes, denoted as $(RuCo)_{NC+SAs}$/N-CNT, in which diluted RuCo alloy nanoparticles coexist with atomically dispersed Ru and Co single atoms (Fig. 12(a)) [12]. The combined effects of Co alloying and single-atom decoration synergistically modulate the electronic structure of Ru, optimizing H adsorption while strengthening OH adsorption (Figs. 12(b) and 12(c)). As a result, the catalyst exhibits a mass activity of 7.35 $A·mg_{Ru}^{-1}$ and delivers a peak power density of 1.98 $W·cm^{-2}$ in fuel cell tests, while maintaining remarkable stability under high CO concentrations (Fig. 12(d)). Its performance substantially surpasses that of commercial Pt/C and PtRu/C catalysts.

Beyond strategies that integrate nanoparticles with single atoms, further efforts have focused on maximizing active-site exposure and enhancing mass transport through precise control of support architecture and coordination environments. Liu et al. employed an ordered porous carbon as the support and introduced dual N/S heteroatom doping to tailor the coordination structure, thereby constructing a Pd single-atom catalyst denoted as Pd_{SA}/N, S-OPC [118]. In this catalyst, Pd forms a stable Pd–N_4 center, while S is distributed in C–S–C configurations in the surrounding framework, collectively modulating the electronic structure of Pd through synergistic electronic effects. This design not only accelerates HOR kinetics by optimizing H adsorption but also significantly improves active-site accessibility and mass transport owing to the ordered porous structure. In a closely related study, Zhang et al. adopted a similar N/S co-doping strategy but utilized porous graphene with in-plane nanopores and long-range electrical conductivity as the support to prepare a Ru single-atom catalyst (RuSA/NSG), featuring a distinctive Ru–N_4–S_2 coordination environment [119]. The synergistic coordination of N and S finely tunes the electronic state of Ru, thereby optimizing the adsorption energies of reaction intermediates.

Beyond tuning the coordination environment via heteroatom-doped supports, introducing dual-atom synergy at active sites has

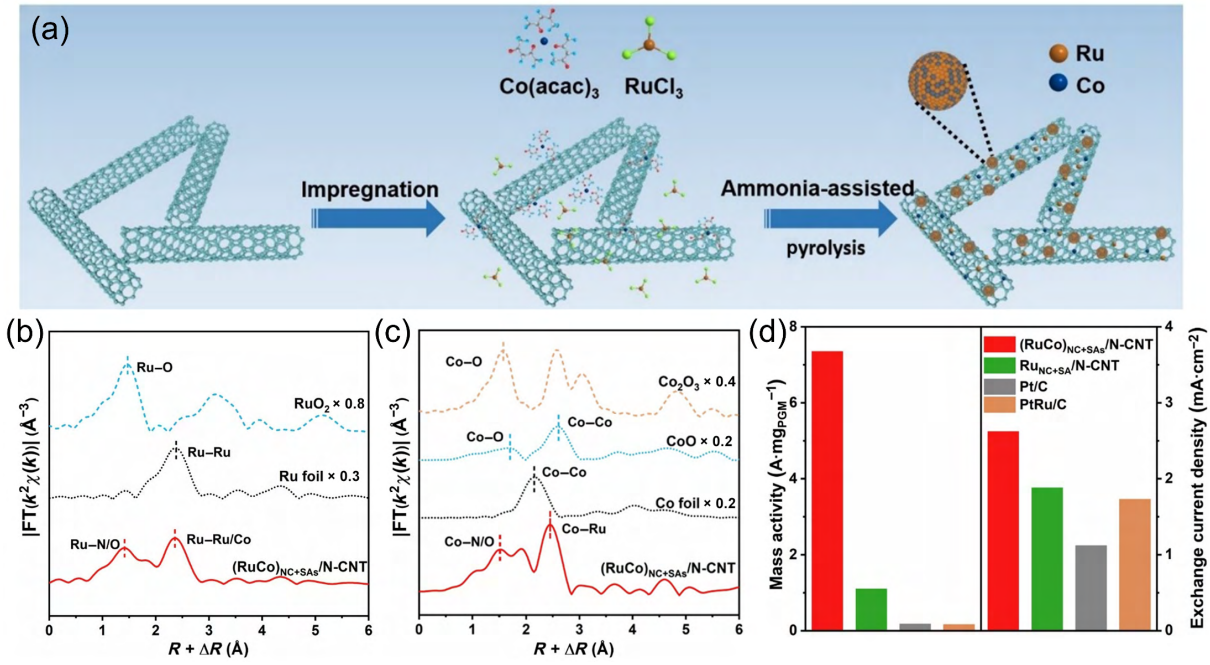

Figure 12 (a) Synthesis and morphological characterizations of $(RuCo)_{NC+SAs}$/N-CNT. The corresponding comparison FT-EXAFS spectra at the (b) Ru K-edge and (c) Co K-edge of $(RuCo)_{NC+SAs}$/N-CNT and reference. (d) j_{km} at 50 mV and j_0 of $(RuCo)_{NC+SAs}$/N-CNT, Ru_{NC+SA}/N-CNT, commercial Pt/C, and PtRu/C. Reproduced with permission from Ref. [12], © Wiley-VCH GmbH 2024.

emerged as a key strategy for enhancing alkaline HOR performance. Studies have demonstrated that combining two metals with atomic-level precision can effectively decouple and optimize individual reaction steps. For instance, Han et al. designed and synthesized a Ru–Ni dual-atom catalyst supported on nitrogen-doped porous carbon (RuNi/NC) through a combination of theoretical calculations and experiments [120]. This material features a well-defined RuN_3–NiN_3 coordination structure, with an interatomic distance of ~ 2.4 Å, uniformly dispersed on a high-surface-area carbon scaffold. Scanning electrochemical microscopy (SECM) revealed that elevated HOR substrate currents occur exclusively in regions containing Ru–Ni dual-atom sites. Meanwhile, *in situ* X-ray absorption near edge structure (XANES) demonstrated that the potential-dependent changes in the Ru K-edge correlate with OH^- adsorption/desorption, whereas variations in Ni electronic structure correspond to H_2 dissociation, directly confirming the synergistic mechanism in which Ru promotes OH^- adsorption, and Ni facilitates H_2 activation.

Similarly, Huang et al. employed a dual-atom strategy to develop a catalyst (Pt_1@Co_1-CN) in which Co single atoms were pre-anchored on nitrogen-doped porous carbon to modulate the electronic structure of adjacent Pt single atoms [121]. Although Co and Pt do not form direct bonds, significant electron transfer occurs via the carbon-nitrogen bridge. Density functional theory (DFT) calculations and XANES spectra indicate that the pre-installed Co atoms act as electron donors, transferring charge to Pt through the support and finely tuning the d-orbital occupancy of Pt, thereby optimizing adsorption of reaction intermediates. As a result, this catalyst exhibits excellent HOR activity and CO tolerance across a wide pH range.

Furthermore, the dual-atom synergy concept can be extended to more complex systems by simultaneously modulating both the active sites and the support to achieve synergistic effects. Jiao et al. prepared Ru_1Pt single-atom alloy nanoparticles supported on W single-atom-modified nitrogen-doped carbon via Joule heating (s-Ru_1Pt@W_1/NC) (Fig. 13(a)) [122]. This system features both short- and long-range cooperative effects: locally, Ru single atoms alloy with Pt nanoparticles; remotely, W single atoms are dispersed within the support. X-ray photoelectron spectroscopy (XPS) spectra and DFT calculations indicate that W atoms accept electrons, inducing electron deficiency in Pt, while Ru incorporation shifts the Pt d-band center upward (Figs. 13(b) and 13(c)). This cooperative effect moderately weakens H adsorption, enhances OH adsorption, and significantly suppresses CO binding. Consequently, s-Ru_1Pt@W_1/NC achieves a mass activity of 7.54 $A{\cdot}mg_{Pt+Ru}^{-1}$ and maintains only 24.60% current decay after 1000 h at 0.05 V vs. RHE (Fig. 13(d)); under 1000 ppm CO/H_2, it retains 82.90% of its initial activity after 5000 s, ranking among the most active alkaline HOR catalysts reported to date.

4.3.2 *Single-atom alloys*

Unlike the aforementioned conventional carbon-supported single atoms, SAA catalysts have attracted widespread attention in recent years. SAAs generally refer to catalysts in which individual metal atoms are dispersed within a host metal, achieving superior catalytic performance through precise atomic-level structural control. In this context, Chen et al. successfully synthesized a Ru_1Pt_n-SAA catalyst via a one-step reduction method with dual H_2 and NO_3^- regulation [123]. Aberration-corrected high-angle annular dark-field scanning transmission electron microscopy (HAADF-STEM) and X-ray absorption fine structure (XAFS) analyses confirmed that Ru exists only in Ru–O bonds (1.55 Å) and Ru–Pt bonds (2.60 Å), with no Ru–Ru bonds, clearly demonstrating the atomic dispersion of Ru within the Pt substrate.

Distinct from the typical alloying of noble metals, another approach is to anchor non-noble metal atoms individually onto a noble metal substrate. This strategy enhances catalytic performance while simultaneously reducing the reliance on costly noble metals.

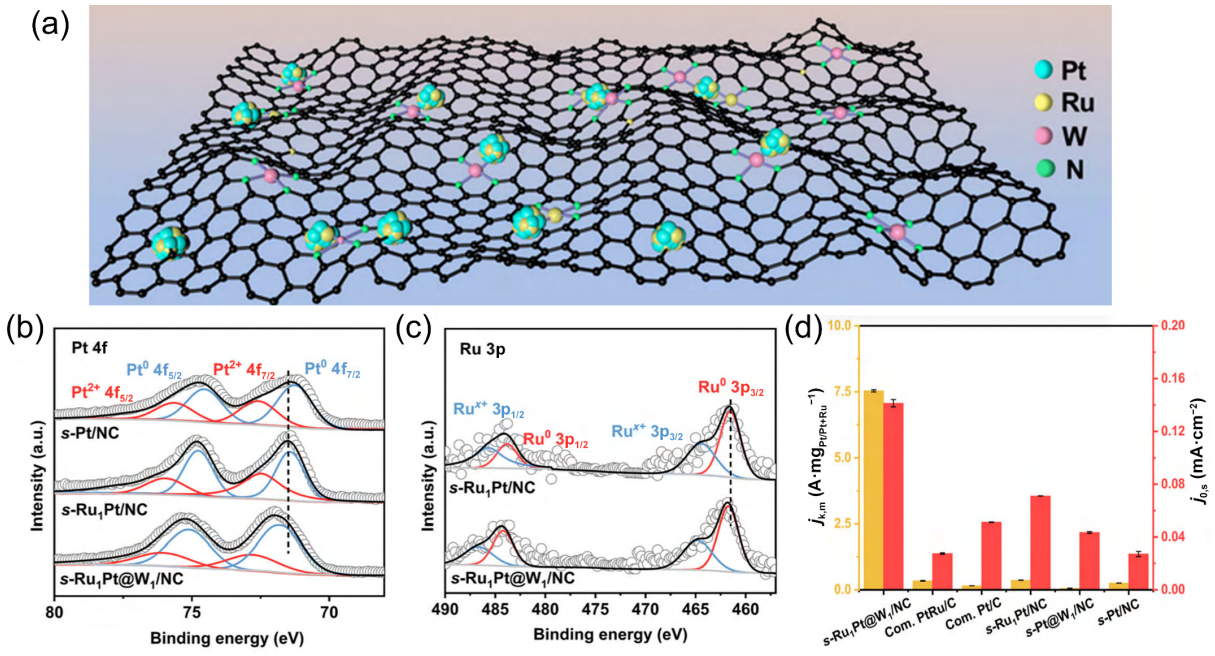

Figure 13 (a) Schematic illustration of *s*-$Ru_1Pt@W_1/NC$ architecture. XPS spectra of (b) Pt 4f and (c) Ru 3p for s-Pt/NC, s-Ru_1Pt/NC, and s-$Ru_1Pt@W_1/NC$. (d) $j_{0,s}$ and $j_{k,m}$ at 0.05 V vs. RHE of *s*-$Ru_1Pt@W_1/NC$ and the references. Reproduced with permission from Ref. [122], © Jiao, W. S. et al. 2025.

For example, Mao et al. deposited Ni single atoms uniformly on the surface of hexagonal close-packed (hcp) Ru nanosheets via a wet-chemistry method, forming $RuNi_1$ nanocrystals (NCs) [124]. The synergistic interaction between isolated Ni single atoms and Ru nanosheets concurrently optimized the HBE and the energy barrier of the Volmer step, resulting in high activity, excellent stability, and Pt-free advantages in alkaline HOR.

Furthermore, atomically precise modification can also be used to tailor specific reaction microenvironments. Ma et al. reported a Mo single-atom-modified Pt nanoparticle catalyst (Mo-Pt/NC) (Fig. 14(a)), in which Mo atoms exert dual functionality: They modulate the d-band center of Pt via electronic effects to weaken H intermediate adsorption (Fig. 14(b)), and simultaneously enhance interfacial water adsorption due to their hydrophilicity, synergistically optimizing the apparent hydrogen adsorption free energy (Fig. 14(c)) [125]. Furthermore, modulation of the local reaction microenvironment can reshape the reaction pathway of the alkaline HOR. Cheng et al. prepared a single-atom Ce-alloyed Ru catalyst (Ce_1Ru/C), in which the much higher oxophilicity of Ce compared to Ru creates an acid-like microenvironment around the Ru active sites [126]. The Ce atoms adsorb abundant OH^-, forming a negatively charged region that repels free OH^-, leaving the neighboring Ru sites in an OH^--deficient state. At these Ru sites, only H is adsorbed and reacts with surrounding adsorbed water to generate the key intermediate hydronium ($H_3O^+_{ad}$), which subsequently neutralizes OH^- in the solution, thereby allowing the alkaline HOR to proceed via an acid-like pathway (Fig. 14(d)). *In situ* Raman spectroscopy and isotope labeling experiments detected characteristic peaks of $H_3O^+_{ad}$ (~ 1800 cm^{-1}) and $HD_2O^+_{ad}$ (~ 2850 cm^{-1}) on the Ce_1Ru/C surface, corroborating this mechanism (Fig. 14(e)). The Ce_1Ru/C catalyst, prepared via a MOF-derived, high-temperature annealing and acid-etching strategy, exhibited outstanding alkaline HOR performance, achieving a mass activity of 40.81 $A{\cdot}mg_{NM}^{-1}$ at 50 mV overpotential with an ultra-low metal loading of only 8.7 $\mu g_{NM}{\cdot}cm^{-2}$, representing one of the highest-performing alkaline HOR catalysts reported to date. Recently, the incorporation of rare-earth single atoms has introduced a new dimension for tuning single-atom alloy systems. Wang et al. employed a vapor-filling and spatially confined reduction strategy to atomically mix Pt nanoclusters (~ 2.6 nm) with rare-earth single atoms (Ln = lanthanum (La), cerium (Ce), praseodymium (Pr), neodymium (Nd), and lutetium (Lu)), yielding a series of $Ln_1Pt@HCS$ catalysts [127]. The rare-earth single atoms selectively adsorb OH due to their strong oxophilicity, while the Pt nanoclusters preferentially adsorb H, achieving spatial separation that prevents adsorption competition. Simultaneously, the rare-earth single atoms induce an upward shift of the Pt d-band center, enhancing OH adsorption and optimizing the binding energies of H and CO. As a result, this series of catalysts demonstrates excellent HOR activity and CO tolerance, validating the generality and effectiveness of this design strategy.

4.3.3 *Transition metal compound-supported single-atom catalysts*

Building upon the progressive maturation of carbon-based and metal-based single-atom support strategies discussed above, TMC, owing to their structural robustness and distinctive electronic properties, have emerged as another important platform for constructing high-performance single-atom catalysts. Unlike conventional N- or S-doped carbon supports, which often induce an elevated oxidation state of the metal centers and a depletion of d-band electrons [143–145], these supports (e.g., carbides and oxides) feature metal-like electrical conductivity [111–114], tunable redox properties [85, 87], and strong interactions with noble metals. As a result, they not only effectively stabilize isolated metal atoms but also actively regulate the electronic states of the active sites from the support side, thereby enabling more favorable catalytic matching.

Taking WC_x with metallic character as a representative example, its broad d band and moderate electronegativity make it an ideal support for constructing low-valence single-atom catalysts. Wang et al. anchored isolated Ru atoms on WC_x, where the weak

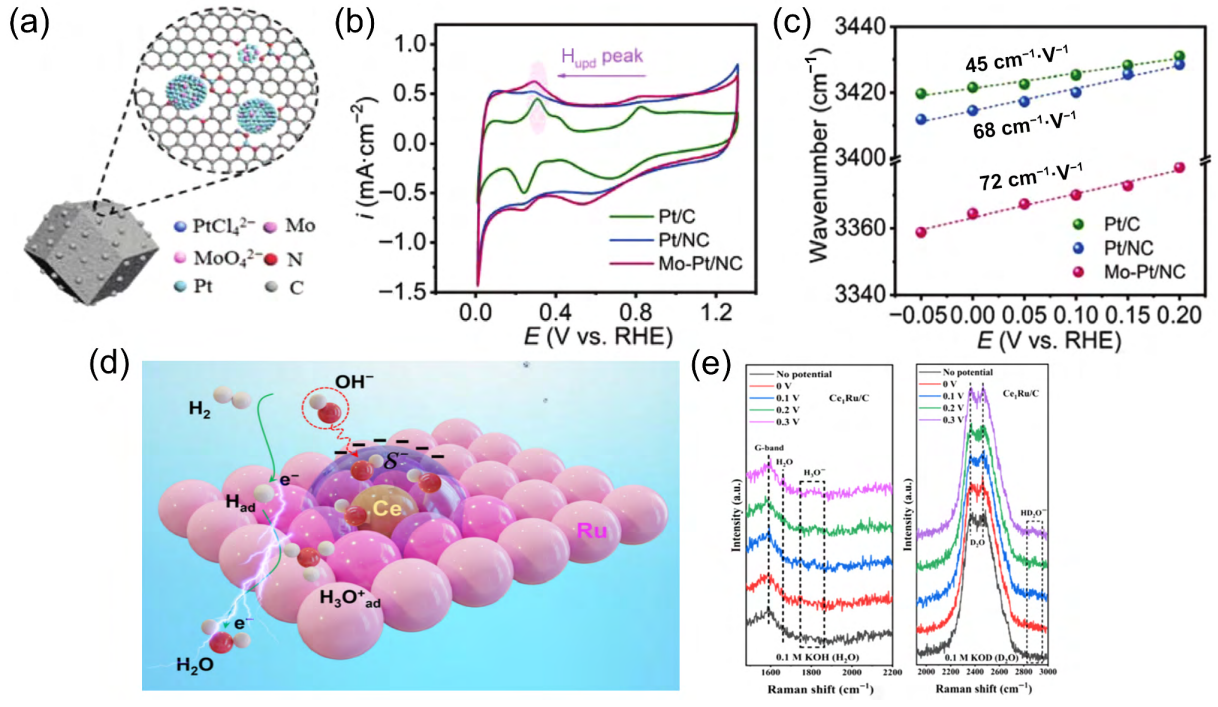

Figure 14 (a) Schematic illustration of Mo-Pt/NC architecture. (b) CV curves of Mo-Pt/NC, Pt/NC, and commercial Pt/C in N_2-saturated 0.1 M KOH solution. (c) Changes in O–H stretching vibration wavenumber of interfacial water for Mo-Pt/NC, Pt/NC, and commercial Pt/C samples with applied potential in H_2-saturated 0.1 M KOH solution. Reproduced with permission from Ref. [125], © Wiley-VCH GmbH 2022. (d) Schematic diagram of the HOR on the surface of the Ce_1Ru/C catalyst under alkaline conditions. (e) *In situ* Raman spectra of Ce_1Ru/C measured in H_2O/KOH (left) and D_2O/KOD (right) solutions. Reproduced with permission from Ref. [126], © American Chemical Society 2024.

coordination environment suppressed the increase in the Ru oxidation state, and maintained it in a near-metallic state [113]. Meanwhile, metal–metal interactions between the support and the single atoms enabled dual-site synergistic catalysis: The low-valence Ru sites optimized H adsorption, while W sites on the WC_x surface strengthened OH adsorption, thereby cooperatively balancing the adsorption energies of H and OH species. As a result, this catalyst delivered a mass activity as high as 7.844 A·mg_{Ru}^{-1} for the alkaline HOR, corresponding to 30.05 times that of commercial Pt/C. Building on this, Park et al. further demonstrated that the low potential of zero charge of WC_{1-x} facilitates efficient interfacial diffusion of OH^- [114]. The surface W–W bridge sites serve as exclusive OH adsorption sites, while the atop Ru single-atom sites preferentially adsorb H, together forming a non-competitive adsorption configuration that effectively avoids the H/OH adsorption competition commonly encountered in conventional single-atom catalysts. In parallel with the WC system, Mo_2C also exhibits outstanding support-induced regulation capabilities. Fang et al. achieved atomic dispersion of Ir on Mo_2C through strong metal–support interactions, yielding Ir_{SA}-Mo_2C/C [111]. The Pt-like electronic structure of Mo_2C maintains the Ir d orbitals in a delocalized metallic state, synergistically optimizing the adsorption free energies of H and OH and thereby markedly enhancing the intrinsic HOR activity. Yang et al. further constructed a yolk–shell Pt_{SA}-Mo_2C-NC catalyst, in which electron transfer between Pt single atoms and Mo_2C downshifts the Pt d-band center, optimizing the adsorption strength of reaction intermediates [112]. Meanwhile, the Mo_2C support exhibits strong CO adsorption and protects Pt sites from poisoning via a "molecular capture" effect, simultaneously improving atomic utilization efficiency and CO tolerance. On the other hand, transition-metal oxides can also serve as effective supports for single-atom catalysts. Cong et al. embedded Ru single atoms together with Ru nanoclusters into an oxygen-vacancy-rich TiO_2 substrate, constructing a "single-atom-cluster" composite active system in which oxygen vacancies regulate the local electronic structure, leading to high activity and stability for the alkaline HOR [85]. Similarly, Zhang et al. prepared Ru single-atom catalysts supported on oxygen-deficient ZrO_{2-x}/C (Ru-SA-ZrO_{2-x}/C) via a facile pyrolysis route, which also exhibited outstanding HOR activity, long-term durability, and strong CO tolerance [87].

In summary, single-atom catalysts for the alkaline HOR have evolved from being predominantly supported on conventional carbon materials to increasingly incorporating metal substrates and transition metal compound supports, reflecting a clear diversification in support design. The central principle underlying these systems lies in the deliberate and controllable interactions between the support and the atomically dispersed active centers, which enable precise regulation of the d-band position, oxidation-state distribution, and local coordination environment of the active sites. While markedly improving atomic utilization efficiency, this strategy also allows fine-tuning of the adsorption behavior of key reaction intermediates and, further, optimization of the interfacial microenvironment, thereby effectively overcoming the limitations of conventional catalysts associated with the activity–stability trade-off and competitive adsorption. Moreover, in many systems, multi-site cooperative mechanisms provide an additional avenue for achieving performance breakthroughs. As the coordination environment of the active sites in the single-atom catalysts is much different from that of the traditional nanoparticle catalysts, their band structures might change in essence, leading to a dramatic change in adsorption of the intermediates. Therefore, the metals previously considered unreactive for HOR (e.g., the metals far away

from the vertex in the HOR volcano plots) might show HOR activity when they are in single-atom forms. It could expand the variety of the HOR catalyst. However, how to precisely control the coordination environment of the metal sites in single-atom catalysts is still in need of further improvement.

5 Summary and outlook

In conclusion, the sluggish kinetics of the alkaline HOR remain one of the key challenges limiting the commercialization of AEMFCs. This review systematically summarizes strategies and recent advances in addressing this challenge through the design of composite catalysts. Studies have shown that both IVB–VIIB transition metal oxides and non-oxide materials, such as carbides and nitrides, can serve as functional components. By leveraging multiple mechanisms—including interfacial electron transfer, oxygen vacancy modulation, construction of dual-functional sites, and facilitation of hydrogen spillover—these materials precisely tune the key-intermediate adsorption and the interfacial water environment, thereby synergistically enhancing the intrinsic HOR activity, high-potential stability, and anti-poisoning performance. This "composite" strategy surpasses the performance limits of conventional alloy materials, demonstrating remarkable universality and design flexibility. In particular, single-atom catalysts, as the atomic-scale manifestation of composite systems, offer a unique perspective for elucidating the intrinsic nature of active sites and their microscopic reaction mechanisms through the precise construction of metal–support interfaces, thereby further extending the concept of composite catalysis to the atomic scale. It should be noted, however, that HOR is a complex, multi-scale process involving multi-level coupling from atomic-scale electron transfer to macroscopic reaction kinetics. Mechanism-based explanations of performance enhancements may hold within specific systems but often lack general applicability. Significant challenges remain in accurately modeling catalyst structures and fundamentally understanding the origins of performance improvements. Future efforts should focus on the development of advanced *in situ* characterization techniques and theoretical simulations to dynamically and in real-time monitor the behavior of reaction intermediates, thereby providing clearer insights into the mechanisms of alkaline HOR. Moreover, although the evaluation of alkaline HOR catalysts has progressed from laboratory-scale three-electrode setups to device-level AEMFCs testing, the pathway toward large-scale commercialization remains to be fully established. Notably, many catalysts that exhibit excellent activity and durability under model conditions often fail to achieve comparable performance in MEA configurations. Therefore, advancing characterization methodologies and promoting the integrated application of high-performance alkaline HOR catalysts represent critical directions for future research in this field.

Data availability

Not applicable.

Acknowledgements

This work is granted by the Hulunbuir University 2025 Doctoral Fund Project (No. 2025BSJJ05) and the National Natural Science Foundation of China (No. 22379004).

Declaration of competing interest

All the contributing authors report no conflict of interests in this work.

Author contribution statement

S. Q. L. conceived the review framework, conducted the literature investigation, curated the data, and prepared the original draft of the manuscript. Q. Q. L. contributed to literature investigation and data curation. Y. N. C. validated and checked the data reported in the manuscript. T. H. L. assisted with literature investigation. W. Z. contributed to visualization, manuscript revision, and provided guidance on responding to reviewers' comments. Z. B. Z. supervised the study, guided the overall framework of the review, and revised the manuscript. All the authors have approved the final manuscript.

Use of AI statement

None.

References

[1] Naseem, K.; Qin, F.; Khalid, F.; Suo, G. Q.; Zahra, T.; Chen, Z. J.; Javed, Z. Essential parts of hydrogen economy: Hydrogen production, storage, transportation and application. *Renewable Sustainable Energy Rev.* **2025**, *210*, 115196.

[2] Hossain Bhuiyan, M. M.; Siddique, Z. Hydrogen as an alternative fuel: A comprehensive review of challenges and opportunities in production, storage, and transportation. *Int. J. Hydrogen Energy* **2025**, *102*, 1026–1044.

[3] Boretti, A.; Pollet, B. G. Hydrogen economy: Paving the path to a sustainable, low-carbon future. *Int. J. Hydrogen Energy* **2024**, *93*, 307–319.

[4] Qasem, N. A. A.; Abdulrahman, G. A. Q. A recent comprehensive review of fuel cells: History, types, and applications. *Int. J. Energy Res.* **2024**, *2024*, 7271748.

[5] Marcelli, L.; Chamoret, D.; François, X.; Meyer, Y.; Candusso, D. Mechanical models and simulations of PEMFCs: A comprehensive review. *Int. J. Hydrogen Energy* **2025**, *136*, 1086–1111.

[6] Sun, Q. D.; Yue, X.; Yu, L. K.; Li, F. Z.; Zheng, Y. W.; Liu, M. T.; Peng, J. Z.; Hu, X. L.; Chen, H. M.; Li, L. et al. Well-defined CO_2 dual-atom catalyst breaks scaling relations of oxygen reduction reaction. *J. Am. Chem. Soc.* **2024**, *146*, 35295–35304.

[7] Wang, Q. C.; Lyu, L.; Hu, X.; Fan, W. Q.; Shang, C. Y.; Huang, Q. R.; Li, Z. P.; Zhou, Z.; Kang, Y. M. Tailoring the surface curvature of the supporting carbon to tune the d-band center of Fe–N–C single-atom catalysts for zinc-urea-air batteries. *Angew. Chem., Int. Ed.* **2025**, *64*, e202422920.

[8] Durst, J.; Siebel, A.; Simon, C.; Hasché, F.; Herranz, J.; Gasteiger, H. A. New insights into the electrochemical hydrogen oxidation and evolution reaction mechanism. *Energy Environ. Sci.* **2014**, *7*, 2255–2260.

[9] Zeng, Y. Z.; Wang, X.; Hu, Y.; Qi, W.; Wang, Z. Q.; Xiao, M. L.; Liu, C. P.; Xing, W.; Zhu, J. B. Research progress of electrocatalysts for hydrogen oxidation reaction in alkaline media. *Carbon Neutralization* **2024**, *3*, 710–736.

[10] Wu, J.; Kang, Z. H.; Zhang, X. Recent progress in alkaline electrocatalytic hydrogen oxidation reaction: Mechanisms, catalysts design and perspectives. *Coord. Chem. Rev.* **2025**, *528*, 216427.

[11] Su, L. X.; Cui, C. X.; Zhou, S. N.; Wu, H.; Zhang, S. K.; Pang, H. Alkaline hydrogen oxidation reaction on ruthenium-based catalysts: From mechanism insights to catalyst advances. *Nano Energy* **2025**, *140*, 111051.

[12] Cui, Z. B.; Ren, Z. H.; Ma, C.; Chen, B. W.; Chen, G. Z.; Lu, R. H.; Zhu, W.; Gan, T.; Wang, Z. Y.; Zhuang, Z. B. et al. Dilute RuCo

alloy synergizing single Ru and Co atoms as efficient and CO-resistant anode catalyst for anion exchange membrane fuel cells. *Angew. Chem., Int. Ed.* **2024**, *63*, e202404761.

[13] Dong, Z. H.; Nan, Y.; Tang, T.; Liu, X. Z.; Fu, J. J.; Pan, H. R.; Jiang, Z.; Ding, L.; Cheng, X.; Zheng, L. R. et al. Synergistically mitigating electron back-donation by single-atomic Fe–N–C and alloying to boost CO-tolerance of Pt in hydrogen oxidation. *ACS Catal.* **2023**, *13*, 7822–7830.

[14] Wang, X. D.; Liu, X. R.; Fang, J. J.; Wang, H. P.; Liu, X. W.; Wang, H. Y.; Chen, C. J.; Wang, Y. S.; Zhang, X. J.; Zhu, W. et al. Tuning the apparent hydrogen binding energy to achieve high-performance Ni-based hydrogen oxidation reaction catalyst. *Nat. Commun.* **2024**, *15*, 1137.

[15] Tian, X. Y.; Ren, R. J.; Wei, F. Y.; Pei, J. J.; Zhuang, Z. B.; Zhuang, L.; Sheng, W. C. Metal–support interaction boosts the stability of Ni-based electrocatalysts for alkaline hydrogen oxidation. *Nat. Commun.* **2024**, *15*, 76.

[16] Zhuang, Z. B.; Giles, S. A.; Zheng, J.; Jenness, G. R.; Caratzoulas, S.; Vlachos, D. G.; Yan, Y. S. Nickel supported on nitrogen-doped carbon nanotubes as hydrogen oxidation reaction catalyst in alkaline electrolyte. *Nat. Commun.* **2016**, *7*, 10141.

[17] Duan, Y.; Zhang, X. L.; Gao, F. Y.; Kong, Y.; Duan, Y.; Yang, X. T.; Yu, X. X.; Wang, Y. R.; Qin, S.; Chen, Z. et al. Interfacial engineering of Ni/V_2O_3 heterostructure catalyst for boosting hydrogen oxidation reaction in alkaline electrolytes. *Angew. Chem., Int. Ed.* **2023**, *135*, e202217275.

[18] Ren, J. T.; Wang, Y. S.; Song, Y. J.; Chen, L.; Yuan, Z. Y. Interface engineering of *in situ* formed nickel hydr(oxy)oxides on nickel nitrides to boost alkaline hydrogen electrocatalysis. *Appl. Catal. B: Environ.* **2022**, *309*, 121279.

[19] Ren, J. T.; Wang, L.; Chen, L.; Song, X. L.; Kong, Q. H.; Wang, H. Y.; Yuan, Z. Y. Interface metal oxides regulating electronic state around nickel species for efficient alkaline hydrogen electrocatalysis. *Small* **2023**, *19*, 2206196.

[20] Ren, J. T.; Wu, X. M.; Liu, T.; Chen, L.; Hao, R.; Song, Y. J.; Liu, Y. P.; Yuan, Z. Y. Interfacing nickel with molybdenum oxides as monolithic catalyst to accelerate alkaline hydrogen electrocatalysis with robust stability. *Appl. Catal. B: Environ.* **2022**, *317*, 121786.

[21] Chen, L.; Wang, H. Y.; Tian, W. W.; Wang, L.; Sun, M. L.; Ren, J. T.; Yuan, Z. Y. Enabling internal electric field in heterogeneous nanosheets to significantly accelerate alkaline hydrogen electrocatalysis. *Small* **2024**, *20*, 2307252.

[22] Zhang, X.; Xie, Y.; Wang, L. Progress and prospect of Pt-based catalysts for electrocatalytic hydrogen oxidation reactions. *Nano Res.* **2024**, *17*, 960–981.

[23] Lv, Q. Q.; Liu, D.; Zhu, W.; Zhuang, Z. B. Iridium-based alkaline hydrogen oxidation reaction electrocatalysts. *Chem.—Eur. J.* **2024**, *30*, e202400838.

[24] Lu, S. Q.; Zhuang, Z. B. Electrocatalysts for hydrogen oxidation and evolution reactions. *Sci. China Mater.* **2016**, *59*, 217–238.

[25] Sheng, W. C.; Gasteiger, H. A.; Shao-Horn, Y. Hydrogen oxidation and evolution reaction kinetics on platinum: Acid vs. alkaline electrolytes. *J. Electrochem. Soc.* **2010**, *157*, B1529–B1536.

[26] Sheng, W. C.; Myint, M.; Chen, J. G.; Yan, Y. S. Correlating the hydrogen evolution reaction activity in alkaline electrolytes with the hydrogen binding energy on monometallic surfaces. *Energy Environ. Sci.* **2013**, *6*, 1509–1512.

[27] Subbaraman, R.; Tripkovic, D.; Strmcnik, D.; Chang, K. C.; Uchimura, M.; Paulikas, A. P.; Stamenkovic, V.; Markovic, N. M. Enhancing hydrogen evolution activity in water splitting by tailoring Li^+–$Ni(OH)_2$–Pt interfaces. *Science* **2011**, *334*, 1256–1260.

[28] Wang, Y. H.; Zheng, S. S.; Yang, W. M.; Zhou, R. Y.; He, Q. F.; Radjenovic, P.; Dong, J. C.; Li, S. N.; Zheng, J. X.; Yang, Z. L. et al. *In situ* Raman spectroscopy reveals the structure and dissociation of interfacial water. *Nature* **2021**, *600*, 81–85.

[29] Nørskov, J. K.; Bligaard, T.; Logadottir, A.; Kitchin, J. R.; Chen, J. G.; Pandelov, S.; Stimming, U. Trends in the exchange current for hydrogen evolution. *J. Electrochem. Soc.* **2005**, *152*, J23–J26.

[30] Zhang, J. T.; Liu, X. Z.; Ji, Y. J.; Liu, X. R.; Su, D.; Zhuang, Z. B.; Chang, Y. C.; Pao, C. W.; Shao, Q.; Hu, Z. W. et al. Atomic-thick metastable phase RhMo nanosheets for hydrogen oxidation catalysis. *Nat. Commun.* **2023**, *14*, 1761.

[31] Xue, Y. R.; Shi, L.; Liu, X. R.; Fang, J. J.; Wang, X. D.; Setzler, B. P.; Zhu, W.; Yan, Y. S.; Zhuang, Z. B. A highly-active, stable and low-cost platinum-free anode catalyst based on RuNi for hydroxide exchange membrane fuel cells. *Nat. Commun.* **2020**, *11*, 5651.

[32] Guan, S. Y.; Liu, Y. Y.; Liu, S. L.; Zhuang, Z. C.; Shen, R. F.; Zhang, H. H.; Liang, E. J.; Fan, Y. P.; Jiang, J. C.; Liu, B. Z. et al. MXene-supported Ru–Ni: A common active site for hydrolysis, hydrogen oxidation, and hydrogenation. *Angew. Chem., Int. Ed.* **2025**, *64*, e202506869.

[33] Basset, J. M.; Pelletier, J. D. A. Predictive approach of heterogeneous catalysis. *Natl. Sci. Rev.* **2018**, *5*, 633–635.

[34] Zhao, J. W.; Wang, H. Y.; Feng, L.; Zhu, J. Z.; Liu, J. X.; Li, W. X. Crystal-phase engineering in heterogeneous catalysis. *Chem. Rev.* **2024**, *124*, 164–209.

[35] Wang, A. Q.; Li, J.; Zhang, T. Heterogeneous single-atom catalysis. *Nat. Rev. Chem.* **2018**, *2*, 65–81.

[36] Ji, S. F.; Chen, Y. J.; Wang, X. L.; Zhang, Z. D.; Wang, D. S.; Li, Y. D. Chemical synthesis of single atomic site catalysts. *Chem. Rev.* **2020**, *120*, 11900–11955.

[37] Liu, J. J.; Yang, J. R.; Dou, Y. H.; Liu, X. W.; Chen, S. H.; Wang, D. S. Deactivation mechanism and mitigation strategies of single-atom site electrocatalysts. *Adv. Mater.* **2025**, *37*, 2420383.

[38] Song, X. Y.; Yang, Q. M.; Zou, K. S.; Xie, Z. Y.; Wang, J.; Ding, W. Intrinsic activity: A critical challenge of alkaline hydrogen oxidation reaction. *Adv. Funct. Mater.* **2025**, *35*, 2414570.

[39] Ren, J. T.; Chen, L.; Wang, H. Y.; Feng, Y.; Yuan, Z. Y. Hydrogen oxidation electrocatalysts for anion-exchange membrane fuel cells: Activity descriptors, stability regulation, and perspectives. *Energy Environ. Sci.* **2024**, *17*, 3960–4009.

[40] Wang, T.; Iriawan, H.; Peng, J. Y.; Rao, R. R.; Huang, B. T.; Zheng, D.; Menga, D.; Aggarwal, A.; Yuan, S.; Eom, J. et al. Confined water for catalysis: Thermodynamic properties and reaction kinetics. *Chem. Rev.* **2025**, *125*, 1420–1467.

[41] Zheng, J.; Sheng, W. C.; Zhuang, Z. B.; Xu, B. J.; Yan, Y. S. Universal dependence of hydrogen oxidation and evolution reaction activity of platinum-group metals on pH and hydrogen binding energy. *Sci. Adv.* **2016**, *2*, e1501602.

[42] Wang, Y.; Wang, G. W.; Li, G. W.; Huang, B.; Pan, J.; Liu, Q.; Han, J. J.; Xiao, L.; Lu, J. T.; Zhuang, L. Pt–Ru catalyzed hydrogen oxidation in alkaline media: Oxophilic effect or electronic effect. *Energy Environ. Sci.* **2015**, *8*, 177–181.

[43] Lu, S. Q.; Zhuang, Z. B. Investigating the influences of the adsorbed species on catalytic activity for hydrogen oxidation reaction in alkaline electrolyte. *J. Am. Chem. Soc.* **2017**, *139*, 5156–5163.

[44] Zheng, J.; Nash, J.; Xu, B. J.; Yan, Y. S. Perspective-towards establishing apparent hydrogen binding energy as the descriptor for hydrogen oxidation/evolution reactions. *J. Electrochem. Soc.* **2018**, *165*, H27–H29.

[45] Sheng, W. C.; Zhuang, Z. B.; Gao, M. R.; Zheng, J.; Chen, J. G.; Yan, Y. S. Correlating hydrogen oxidation and evolution activity on platinum at different pH with measured hydrogen binding energy. *Nat. Commun.* **2015**, *6*, 5848.

[46] Strmcnik, D.; Uchimura, M.; Wang, C.; Subbaraman, R.; Danilovic, N.; Van Der Vliet, D.; Paulikas, A. P.; Stamenkovic, V. R.; Markovic, N. M. Improving the hydrogen oxidation reaction rate by promotion of hydroxyl adsorption. *Nat. Chem.* **2013**, *5*, 300–306.

[47] McCrum, I. T.; Koper, M. T. M. The role of adsorbed hydroxide in hydrogen evolution reaction kinetics on modified platinum. *Nat. Energy* **2020**, *5*, 891–899.

[48] Lin, X. M.; Wang, X. T.; Deng, Y. L.; Chen, X.; Chen, H. N.; Radjenovic, P. M.; Zhang, X. G.; Wang, Y. H.; Dong, J. C.; Tian, Z. Q. et al. *In situ* probe of the hydrogen oxidation reaction intermediates on PtRu a bimetallic catalyst surface by core–shell nanoparticle-enhanced Raman spectroscopy. *Nano Lett.* **2022**, *22*, 5544–5552.

[49] Shi, G. Y.; Yano, H.; Tryk, D. A.; Iiyama, A.; Uchida, H. Highly

active, CO-tolerant, and robust hydrogen anode catalysts: Pt–M (M = Fe, Co, Ni) alloys with stabilized Pt-skin layers. *ACS Catal.* **2017**, *7*, 267–274.

[50] Yang, Y.; Gao, F. Y.; Zhang, X. L.; Qin, S.; Zheng, L. R.; Wang, Y. H.; Liao, J.; Yang, Q.; Gao, M. R. Suppressing electron back-donation for a highly CO-tolerant fuel cell anode catalyst via cobalt modulation. *Angew. Chem., Int. Ed.* **2022**, *61*, e202208040.

[51] Wang, X. N.; Zhao, L. M.; Li, X. J.; Liu, Y.; Wang, Y. S.; Yao, Q. F.; Xie, J. P.; Xue, Q. Z.; Yan, Z. F.; Yuan, X. et al. Atomic-precision Pt_6 nanoclusters for enhanced hydrogen electro-oxidation. *Nat. Commun.* **2022**, *13*, 1596.

[52] Liu, Z. F.; Jackson, G. S.; Eichhorn, B. W. PtSn intermetallic, core–shell, and alloy nanoparticles as CO-tolerant electrocatalysts for H_2 oxidation. *Angew. Chem., Int. Ed.* **2010**, *49*, 3173–3176.

[53] Zhou, Y. Y.; Xie, Z. Y.; Jiang, J. X.; Wang, J.; Song, X. Y.; He, Q.; Ding, W.; Wei, Z. D. Lattice-confined Ru clusters with high CO tolerance and activity for the hydrogen oxidation reaction. *Nat. Catal.* **2020**, *3*, 454–462.

[54] Dong, Y. T.; Zhang, Z. M.; Yan, W.; Hu, X. R.; Zhan, C. H.; Xu, Y.; Huang, X. Q. Pb-modified ultrathin RuCu nanoflowers for active, stable, and CO-resistant alkaline electrocatalytic hydrogen oxidation. *Angew. Chem., Int. Ed.* **2023**, *62*, e202311722.

[55] Zhang, B. X.; Wang, J. M.; Liu, G. M.; Weiss, C. M.; Liu, D. Q.; Chen, Y. P.; Xia, L. X.; Zhou, P.; Gao, M. X.; Liu, Y. F. et al. A strongly coupled Ru–CrO_x cluster–cluster heterostructure for efficient alkaline hydrogen electrocatalysis. *Nat. Catal.* **2024**, *7*, 441–451.

[56] Sebastián-Pascual, P.; Herzog, A.; Zhang, Y. R.; Shao-Horn, Y.; Escudero-Escribano, M. Electrolyte effects in proton–electron transfer reactions and implications for renewable fuels and chemicals synthesis. *Nat. Catal.* **2025**, *8*, 986–999.

[57] Yuan, Y. L.; Li, J.; Zhu, Y. T.; Qiao, Y.; Kang, Z. Y.; Wang, Z. T.; Tian, X. L.; Huang, H. W.; Lai, W. C. Water in electrocatalysis. *Angew. Chem., Int. Ed.* **2025**, *64*, e202425590.

[58] Velasco-Velez, J. J.; Wu, C. H.; Pascal, T. A.; Wan, L. F.; Guo, J. H.; Prendergast, D.; Salmeron, M. The structure of interfacial water on gold electrodes studied by X-ray absorption spectroscopy. *Science* **2014**, *346*, 831–834.

[59] Li, M. T.; Li, L.; Huang, X.; Qi, X. Q.; Deng, M. M.; Jiang, S. K.; Wei, Z. D. Platinum–water interaction induced interfacial water orientation that governs the pH-dependent hydrogen oxidation reaction. *J. Phys. Chem. Lett.* **2022**, *13*, 10550–10557.

[60] Yang, J.; Dettori, R.; Nunes, J. P. F.; List, N. H.; Biasin, E.; Centurion, M.; Chen, Z. J.; Cordones, A. A.; Deponte, D. P.; Heinz, T. F. et al. Direct observation of ultrafast hydrogen bond strengthening in liquid water. *Nature* **2021**, *596*, 531–535.

[61] Li, P.; Jiang, Y. L.; Hu, Y. C.; Men, Y.; Liu, Y. W.; Cai, W. B.; Chen, S. L. Hydrogen bond network connectivity in the electric double layer dominates the kinetic pH effect in hydrogen electrocatalysis on Pt. *Nat. Catal.* **2022**, *5*, 900–911.

[62] Shen, L. F.; Lu, B. A.; Li, Y. Y.; Liu, J.; Huang-fu, Z. C.; Peng, H.; Ye, J. Y.; Qu, X. M.; Zhang, J. M.; Li, G. et al. Interfacial structure of water as a new descriptor of the hydrogen evolution reaction. *Angew. Chem., Int. Ed.* **2020**, *59*, 22397–22402.

[63] Huang, J.; Li, P.; Chen, S. L. Quantitative understanding of the sluggish kinetics of hydrogen reactions in alkaline media based on a microscopic Hamiltonian model for the Volmer step. *J. Phys. Chem. C* **2019**, *123*, 17325–17334.

[64] Brini, E.; Fennell, C. J.; Fernandez-Serra, M.; Hribar-Lee, B.; Lukšič, M.; Dill, K. A. How water's properties are encoded in its molecular structure and energies. *Chem. Rev.* **2017**, *117*, 12385–12414.

[65] Ledezma-Yanez, I.; Wallace, W. D. Z.; Sebastián-Pascual, P.; Climent, V.; Feliu, J. M.; Koper, M. T. M. Interfacial water reorganization as a pH-dependent descriptor of the hydrogen evolution rate on platinum electrodes. *Nat. Energy* **2017**, *2*, 17031.

[66] Garcia-Araez, N.; Climent, V.; Feliu, J. Potential-dependent water orientation on Pt (111), Pt (100), and Pt (110), as inferred from laser-pulsed experiments. Electrostatic and chemical effects. *J. Phys. Chem. C* **2009**, *113*, 9290–9304.

[67] Rebollar, L.; Intikhab, S.; Oliveira, N. J.; Yan, Y. S.; Xu, B. J.; McCrum, I. T.; Snyder, J. D.; Tang, M. H. "Beyond adsorption" descriptors in hydrogen electrocatalysis. *ACS Catal.* **2020**, *10*, 14747–14762.

[68] Li, C. Y.; Le, J. B.; Wang, Y. H.; Chen, S.; Yang, Z. L.; Li, J. F.; Cheng, J.; Tian, Z. Q. *In situ* probing electrified interfacial water structures at atomically flat surfaces. *Nat. Mater.* **2019**, *18*, 697–701.

[69] Huang, B. T.; Rao, R. R.; You, S. F.; Hpone Myint, K.; Song, Y. Z.; Wang, Y. M.; Ding, W. D.; Giordano, L.; Zhang, Y. R.; Wang, T. et al. Cation- and pH-dependent hydrogen evolution and oxidation reaction kinetics. *JACS Au* **2021**, *1*, 1674–1687.

[70] Tian, Y.; Huang, B. T.; Song, Y. Z.; Zhang, Y. R.; Guan, D.; Hong, J. N.; Cao, D. Y.; Wang, E. G.; Xu, L. M.; Shao-Horn, Y. et al. Effect of ion-specific water structures at metal surfaces on hydrogen production. *Nat. Commun.* **2024**, *15*, 7834.

[71] Su, L. X.; Chen, J. X.; Yang, F. L.; Li, P.; Jin, Y. M.; Luo, W.; Chen, S. L. Electric-double-layer origin of the kinetic pH effect of hydrogen electrocatalysis revealed by a universal hydroxide adsorption-dependent inflection-point behavior. *J. Am. Chem. Soc.* **2023**, *145*, 12051–12058.

[72] Zhao, K. Y.; Chang, X. X.; Su, H. S.; Nie, Y. M.; Lu, Q.; Xu, B. J. Enhancing hydrogen oxidation and evolution kinetics by tuning the interfacial hydrogen-bonding environment on functionalized platinum surfaces. *Angew. Chem., Int. Ed.* **2022**, *61*, e202207197.

[73] Savoj, R.; Agnew, H.; Zhou, R. H.; Paesani, F. Molecular insights into the influence of ions on the water structure. I. Alkali metal ions in solution. *J. Phys. Chem. B* **2024**, *128*, 1953–1962.

[74] Intikhab, S.; Rebollar, L.; Li, Y. W.; Pai, R.; Kalra, V.; Tang, M. H.; Snyder, J. D. Caffeinated interfaces enhance alkaline hydrogen electrocatalysis. *ACS Catal.* **2020**, *10*, 6798–6802.

[75] Zhao, K. Y.; Yu, H.; Xiong, H. C.; Lu, Q.; Gao, Y. Q.; Xu, B. J. Action at a distance: Organic cation induced long range organization of interfacial water enhances hydrogen evolution and oxidation kinetics. *Chem. Sci.* **2023**, *14*, 11076–11087.

[76] Shirasawa, T.; Masuda, T.; Voegeli, W.; Arakawa, E.; Kamezawa, C.; Takahashi, T.; Uosaki, K.; Matsushita, T. Fast structure determination of electrode surfaces for investigating electrochemical dynamics using wavelength-dispersive X-ray crystal truncation rod measurements. *J. Phys. Chem. C* **2017**, *121*, 24726–24732.

[77] Tanaka, S.; Tajiri, H.; Sakata, O.; Hoshi, N.; Nakamura, M. Interfacial structure of Pt (110) electrode during hydrogen evolution reaction in alkaline solutions. *J. Phys. Chem. Lett.* **2022**, *13*, 8403–8408.

[78] Zhang, J. F.; Zhu, W. K.; Huang, T.; Zheng, C. Y.; Pei, Y. B.; Shen, G. Q.; Nie, Z. X.; Xiao, D.; Yin, Y.; Guiver, M. D. Recent insights on catalyst layers for anion exchange membrane fuel cells. *Adv. Sci.* **2021**, *8*, 2100284.

[79] Mao, J. Y.; Wang, X. C.; Nie, Y. T.; Chen, X. Q.; Hu, C.; Zhu, A. M.; Chen, W. P.; Xie, Z. X.; Zhang, Q. G. Anion exchange ionomers for anion exchange membrane fuel cells: Properties, advances, and future directions. *Int. J. Hydrogen Energy* **2025**, *196*, 152593.

[80] Ponce-González, J.; Whelligan, D. K.; Wang, L. Q.; Bance-Soualhi, R.; Wang, Y.; Peng, Y. Q.; Peng, H. Q.; Apperley, D. C.; Sarode, H. N.; Pandey, T. P. et al. High performance aliphatic-heterocyclic benzyl-quaternary ammonium radiation-grafted anion-exchange membranes. *Energy Environ. Sci.* **2016**, *9*, 3724–3735.

[81] Varcoe, J. R.; Atanassov, P.; Dekel, D. R.; Herring, A. M.; Hickner, M. A.; Kohl, P. A.; Kucernak, A. R.; Mustain, W. E.; Nijmeijer, K.; Scott, K. et al. Anion-exchange membranes in electrochemical energy systems. *Energy Environ. Sci.* **2014**, *7*, 3135–3191.

[82] Pan, J.; Chen, C.; Li, Y.; Wang, L.; Tan, L. S.; Li, G. W.; Tang, X.; Xiao, L.; Lu, J. T.; Zhuang, L. Constructing ionic highway in alkaline polymer electrolytes. *Energy Environ. Sci.* **2014**, *7*, 354–360.

[83] Jiang, J. X.; Tao, S. C.; He, Q.; Wang, J.; Zhou, Y. Y.; Xie, Z. Y.; Ding, W.; Wei, Z. D. Interphase-oxidized ruthenium metal with half-

filled d-orbitals for hydrogen oxidation in an alkaline solution. *J. Mater. Chem. A* **2020**, *8*, 10168–10174.

[84] Jin, X.; Zhang, X. Y.; Yang, B.; Zheng, X. Z.; Gao, M. X.; Pan, H. G.; Sun, W. P. Engineering intense Ru–TiO_2 interaction for robust hydrogen oxidation reaction. *J. Mater. Chem. A* **2025**, *13*, 20404–20411.

[85] Cong, Y. Y.; Liu, M. L.; Chen, L. Y.; Qi, Y. R.; Zhang, L. M.; Zhao, Q. P.; Li, C. L.; Wang, H. B. Ru-embedded TiO_{2-x} with rich Ru–Ti bonds and triggered oxygen vacancies for boosted and sustained hydrogen oxidation and evolution electrocatalysis in alkaline medium. *Chem. Eng. J.* **2024**, *501*, 157669.

[86] Li, X. J.; Tong, Y. F.; Luo, W. Y.; Wang, X. N.; Zhao, L. M.; Liu, P. Y.; Cai, T. H.; Cui, Y. P.; Yan, Z. F.; Xing, W. Bidirectional electron relay at TiN–TiO_2 interfaces enables oxidation-resistant Ru for high-potential hydrogen oxidation catalysis. *Angew. Chem., Int. Ed.* **2025**, *64*, e202512285.

[87] Zhang, X.; Wang, C.; Cao, W.; Zhu, Q.; Cheng, C.; Zheng, J.; Zhang, H.; Guo, Y.; Huang, S.; Yu, Y. et al. Ru single atoms anchored on oxygen-vacancy-rich ZrO_{2-x}/C for synergistically enhanced hydrogen oxidation. *Adv. Sci.* **2025**, *12*, 2413569.

[88] Ghoshal, S.; Jia, Q. Y.; Bates, M. K.; Li, J. K.; Xu, C. C.; Gath, K.; Yang, J.; Waldecker, J.; Che, H. Y.; Liang, W. T. et al. Tuning Nb–Pt interactions to facilitate fuel cell electrocatalysis. *ACS Catal.* **2017**, *7*, 4936–4946.

[89] Wang, P. C.; Yang, Y.; Zheng, W.; Cheng, Z. Y.; Wang, C. L.; Chen, S.; Wang, D. D.; Yang, J. H.; Shi, H. D.; Meng, P. et al. V–O species-doped carbon frameworks loaded with Ru nanoparticles as highly efficient and CO-tolerant catalysts for alkaline hydrogen oxidation. *J. Am. Chem. Soc.* **2023**, *145*, 27867–27876.

[90] Zhang, B. X.; Zhang, B. H.; Zhao, G. Q.; Wang, J. M.; Liu, D. Q.; Chen, Y. P.; Xia, L. X.; Gao, M. X.; Liu, Y. F.; Sun, W. P. et al. Atomically dispersed chromium coordinated with hydroxyl clusters enabling efficient hydrogen oxidation on ruthenium. *Nat. Commun.* **2022**, *13*, 5894.

[91] Li, M. T.; Xie, Z. Y.; Zheng, X. Q.; Li, L.; Li, J.; Ding, W.; Wei, Z. D. Revealing the regulation mechanism of Ir–MoO_2 interfacial chemical bonding for improving hydrogen oxidation reaction. *ACS Catal.* **2021**, *11*, 14932–14940.

[92] Luo, H.; Wang, K.; Lin, F. X.; Lv, F.; Zhou, J. H.; Zhang, W. Y.; Wang, D. W.; Zhang, W. S.; Zhang, Q. H.; Gu, L. et al. Amorphous MoO_x with high oxophilicity interfaced with PtMo alloy nanoparticles boosts anti-CO hydrogen electrocatalysis. *Adv. Mater.* **2023**, *35*, 2211854.

[93] Samanta, R.; Manna, B. K.; Trivedi, R.; Chakraborty, B.; Barman, S. Hydrogen spillover enhances alkaline hydrogen electrocatalysis on interface-rich metallic Pt-supported MoO_3. *Chem. Sci.* **2024**, *15*, 364–378.

[94] Fu, L. H.; Yang, F. L.; Hu, Y. C.; Li, Y. B.; Chen, S. L.; Luo, W. Discrepant roles of adsorbed OH* species on $IrWO_x$ for boosting alkaline hydrogen electrocatalysis. *Sci. Bull.* **2020**, *65*, 1735–1742.

[95] Liu, H.; Zhang, Z.; Li, M. X.; Li, Y. P.; Kuang, Y.; Sun, X. M. Ru-doped WO_3 enabling efficient hydrogen oxidation reaction in alkaline media. *Nanoscale* **2023**, *15*, 12064–12070.

[96] Cheng, Z. Y.; Yang, Y.; Wang, P. C.; Wang, P. C.; Yang, J. H.; Wang, D. D.; Chen, Q. W. Optimizing hydrogen and hydroxyl adsorption over $Ru/WO_{2.9}$ metal/metalloid heterostructure electrocatalysts for highly efficient and stable hydrogen oxidation reactions in alkaline media. *Small* **2024**, *20*, 2307780.

[97] Zheng, X. Z.; Zhang, S. X.; Zheng, X. Y.; Zhuang, Z. B.; Gao, M. X.; Liu, Y. F.; Pan, H. G.; Sun, W. P. Cluster-scale multisite interface reinforces ruthenium-based anode catalysts for alkaline anion exchange membrane fuel cells. *Adv. Mater.* **2025**, *37*, 2502127.

[98] Cruz-Reyes, I.; Trujillo-Navarrete, B.; García-Tapia, K.; Salazar-Gastélum, M. I.; Paraguay-Delgado, F.; Félix-Navarro, R. M. Pd/MnO_2 as a bifunctional electrocatalyst for potential application in alkaline fuel cells. *Fuel* **2020**, *279*, 118470.

[99] Zhang, S. Q.; Ren, R. J.; Cao, J.; Zhang, D. Z.; Bai, J. S.; Han, C.; Xiao, L.; Zhuang, L.; Song, P.; Xu, W. L. Ru-MnO heterostructure clusters toward efficient and CO-tolerant alkaline hydrogen oxidation reaction. *Adv. Energy Mater.* **2025**, *15*, 2404266.

[100] Shi, H. D.; Yang, Y.; Meng, P.; Yang, J. H.; Zheng, W.; Wang, P. C.; Zhang, Y. L.; Chen, X. Y.; Cheng, Z. Y.; Zong, C. C. et al. Local charge transfer unveils antideactivation of Ru at high potentials for the alkaline hydrogen oxidation reaction. *J. Am. Chem. Soc.* **2024**, *146*, 16619–16629.

[101] Pagliaro, M. V.; Wen, C. L.; Sa, B.; Liu, B. Y.; Bellini, M.; Bartoli, F.; Sahoo, S.; Singh, R. K.; Alpay, S. P.; Miller, H. A. et al. Improving alkaline hydrogen oxidation activity of palladium through interactions with transition-metal oxides. *ACS Catal.* **2022**, *12*, 10894–10904.

[102] Wang, R. Y.; Li, D. G.; Maurya, S.; Kim, Y. S.; Wu, Y. M.; Liu, Y. Z.; Strmcnik, D.; Markovic, N. M.; Stamenkovic, V. R. Ultrafine Pt cluster and RuO_2 heterojunction anode catalysts designed for ultra-low Pt-loading anion exchange membrane fuel cells. *Nanoscale Horiz.* **2020**, *5*, 316–324.

[103] Zhang, X.; Xia, L. X.; Zhao, G. Q.; Zhang, B. X.; Chen, Y. P.; Chen, J.; Gao, M. X.; Jiang, Y. Z.; Liu, Y. F.; Pan, H. G. et al. Fast and durable alkaline hydrogen oxidation reaction at the electron-deficient ruthenium–ruthenium oxide interface. *Adv. Mater.* **2023**, *35*, 2208821.

[104] Yang, J. H.; Wang, P. C.; Meng, P.; Shi, H. D.; Cheng, Z. Y.; Yang, Y.; Zhang, Y. L.; Chen, X. Y.; Lin, X.; Fan, D. G. et al. Hydrogen stored in Ru/SnO_2 induce alkaline hydrogen oxidation reactions in a wide potential range. *J. Mater. Chem. A* **2025**, *13*, 20488–20495.

[105] Miller, H. A.; Lavacchi, A.; Vizza, F.; Marelli, M.; Di Benedetto, F.; D'Acapito, F.; Paska, Y.; Page, M.; Dekel, D. R. A Pd/C-CeO_2 anode catalyst for high-performance platinum-free anion exchange membrane fuel cells. *Angew. Chem., Int. Ed.* **2016**, *55*, 6004–6007.

[106] Yu, H. R.; Davydova, E. S.; Ash, U.; Miller, H. A.; Bonville, L.; Dekel, D. R.; Maric, R. Palladium-ceria nanocatalyst for hydrogen oxidation in alkaline media: Optimization of the Pd–CeO_2 interface. *Nano Energy* **2019**, *57*, 820–826.

[107] Wang, M. M.; Yang, L.; Qiu, Z. N.; Lu, P.; Sun, H. M.; Chen, J.; Sun, J. C.; Li, C. P. Synergistic Ru/CeO_2 heterostructure for alkaline hydrogen oxidation with high activity and CO tolerance. *Int. J. Hydrogen Energy* **2023**, *48*, 34355–34362.

[108] Cheng, Z. Y.; Yang, Y.; Yang, J. H.; Chen, S.; Wang, P. C.; Wang, P. C.; Tong, H. G.; Wang, C. L.; Chen, Q. W. Oxygen-vacancy-rich CeO_2/Ru nanoparticles enable a high-performance catalyst for alkaline hydrogen oxidation. *J. Mater. Chem. A* **2024**, *12*, 4240–4248.

[109] Liu, D. Q.; Luo, Z. X.; Zhang, B. X.; Zhao, G. Q.; Guo, W.; Chen, J.; Gao, M. X.; Liu, Y. F.; Pan, H. G.; Sun, W. P. Tailoring interfacial charge transfer of epitaxially grown Ir clusters for boosting hydrogen oxidation reaction. *Adv. Energy Mater.* **2023**, *13*, 2202913.

[110] Hamo, E. R.; Singh, R. K.; Douglin, J. C.; Chen, S. A.; Hassine, M. B.; Carbo-Argibay, E.; Lu, S. F.; Wang, H. N.; Ferreira, P. J.; Rosen, B. A. et al. Carbide-supported PtRu catalysts for hydrogen oxidation reaction in alkaline electrolyte. *ACS Catal.* **2021**, *11*, 932–947.

[111] Fang, J. J.; Wang, H. Y.; Dang, Q.; Wang, H.; Wang, X. D.; Pei, J. J.; Xu, Z. Y.; Chen, C. J.; Zhu, W.; Li, H. et al. Atomically dispersed iridium on Mo_2C as an efficient and stable alkaline hydrogen oxidation reaction catalyst. *Nat. Commun.* **2024**, *15*, 4236.

[112] Yang, X. K.; Yu, W. J.; Zhang, Y. F.; Qiao, C. P.; Liu, L. L.; Zhang, Y. F.; Li, Q. R.; Mou, M. F.; Wang, R. T.; Yuan, X. S. et al. Enhancing CO tolerance via molecular trapping effect: Single-atom Pt anchored on Mo_2C for efficient alkaline hydrogen oxidation reaction. *J. Colloid Interface Sci.* **2025**, *692*, 137489.

[113] Wang, L. Q.; Xu, Z. P.; Kuo, C. H.; Peng, J.; Hu, F.; Li, L. L.; Chen, H. Y.; Wang, J. Z.; Peng, S. J. Stabilizing low-valence single atoms by constructing metalloid tungsten carbide supports for efficient hydrogen oxidation and evolution. *Angew. Chem., Int. Ed.* **2023**, *62*, e202311937.

[114] Park, J.; Kim, H.; Kim, S.; Yi, S. Y.; Min, H.; Choi, D.; Lee, S.; Kim, J.; Lee, J. Boosting alkaline hydrogen oxidation activity of Ru single-atom through promoting hydroxyl adsorption on Ru/WC_{1-x} interfaces. *Adv. Mater.* **2024**, *36*, 2308899.

[115] Su, L. X.; Jin, Y. M.; Gong, D.; Ge, X.; Zhang, W.; Fan, X. R.; Luo, W. The role of discrepant reactive intermediates on Ru–Ru_2P heterostructure for pH-universal hydrogen oxidation reaction. *Angew. Chem., Int. Ed.* **2023**, *62*, e202215585.
[116] Jin, Y. M.; Han, Z. X.; Luo, W. MoN supported Pt nanocluster catalysts with regulated interfacial water structures for boosting alkaline hydrogen oxidation reaction. *Adv. Funct. Mater.* **2025**, *35*, 2501377.
[117] Ni, W. Y.; Meibom, J. L.; Hassan, N. U.; Chang, M.; Chu, Y. C.; Krammer, A.; Sun, S. L.; Zheng, Y. W.; Bai, L. C.; Ma, W. C. et al. Synergistic interactions between PtRu catalyst and nitrogen-doped carbon support boost hydrogen oxidation. *Nat. Catal.* **2023**, *6*, 773–783.
[118] Liu, H. X.; Fu, J. T.; Li, H. Y.; Sun, J. Q.; Liu, X. J.; Qiu, Y.; Peng, X. Y.; Liu, Y. F.; Bao, H. H.; Zhuo, L. C. et al. Single palladium site in ordered porous heteroatom-doped carbon for high-performance alkaline hydrogen oxidation. *Appl. Catal. B: Environ.* **2022**, *306*, 121029.
[119] Zhang, Z.; Ni, L. W.; Liu, H. J.; Zhao, Z. L.; Yuan, X. Z.; Li, H. Accelerated kinetics of alkaline hydrogen evolution/oxidation reactions on dispersed ruthenium sites through N and S dual coordination. *Sci. China: Chem.* **2022**, *65*, 611–618.
[120] Han, L. L.; Ou, P. F.; Liu, W.; Wang, X.; Wang, H. T.; Zhang, R.; Pao, C. W.; Liu, X. J.; Pong, W. F.; Song, J. et al. Design of Ru–Ni diatomic sites for efficient alkaline hydrogen oxidation. *Sci. Adv.* **2022**, *8*, eabm3779.
[121] Huang, Z. Y.; Lu, R. H.; Zhang, Y. Z.; Chen, W.; Chen, G. Z.; Ma, C.; Wang, Z. Y.; Han, Y. H.; Huang, W. A highly efficient pH-universal HOR catalyst with engineered electronic structures of single Pt sites by isolated Co atoms. *Adv. Funct. Mater.* **2023**, *33*, 2306333.
[122] Jiao, W. S.; Ren, Z. H.; Cui, Z. B.; Ma, C.; Shang, Z. A.; Chen, G. Z.; Lu, R. H.; Gan, T.; Wang, Z. Y.; Xiong, Y. et al. All-round enhancement induced by oxophilic single Ru and W atoms for alkaline hydrogen oxidation of tiny Pt nanoparticles. *Nat. Commun.* **2025**, *16*, 883.
[123] Chen, L. G.; Liang, X.; Wang, D. S.; Yang, Z. B.; He, C. T.; Zhao, W.; Pei, J. J.; Xue, Y. R. Platinum–ruthenium single atom alloy as a bifunctional electrocatalyst toward methanol and hydrogen oxidation reactions. *ACS Appl. Mater. Interfaces* **2022**, *14*, 27814–27822.
[124] Mao, J. J.; He, C. T.; Pei, J. J.; Liu, Y.; Li, J.; Chen, W. X.; He, D. S.; Wang, D. S.; Li, Y. D. Isolated Ni atoms dispersed on Ru nanosheets: High-performance electrocatalysts toward hydrogen oxidation reaction. *Nano Lett.* **2020**, *20*, 3442–3448.
[125] Ma, M.; Li, G.; Yan, W.; Wu, Z. Z.; Zheng, Z. P.; Zhang, X. B.; Wang, Q. X.; Du, G. F.; Liu, D. Y.; Xie, Z. X. et al. Single-atom molybdenum engineered platinum nanocatalyst for boosted alkaline hydrogen oxidation. *Adv. Energy Mater.* **2022**, *12*, 2103336.
[126] Cheng, Z. Y.; Yang, Y.; Zheng, F. C.; Chen, S.; Wang, P. C.; Wang, P. C.; Huang, H.; Wang, C. L.; Wang, D. D.; Chen, Q. W. Fast kinetics of hydrogen oxidation reaction on single-atom Ce-alloyed Ru in alkaline electrolytes. *ACS Catal.* **2024**, *14*, 3845–3854.
[127] Wang, X. N.; Tong, Y. F.; Feng, W. T.; Liu, P. Y.; Li, X. J.; Cui, Y. P.; Cai, T. H.; Zhao, L. M.; Xue, Q. Z.; Yan, Z. F. et al. Embedding oxophilic rare-earth single atom in platinum nanoclusters for efficient hydrogen electro-oxidation. *Nat. Commun.* **2023**, *14*, 3767.
[128] Wang, X. Y.; Wei, W. J.; Zhou, S. Y.; Pan, Y. Z.; Yang, J. R.; Gan, T.; Zhuang, Z. C.; Li, W. H.; Zhang, X.; Pan, Y. M. et al. Phosphorus-doped single atom copper catalyst as a redox mediator in the cathodic reduction of quinazolinones. *Angew. Chem., Int. Ed.* **2025**, *64*, e202505085.
[129] Yang, Y.; Zhang, W. J.; Wu, G. C.; Huang, Q.; Wen, J. H.; Wang, D. S.; Liu, M. Y. Electronic structure tuning in Cu–Co dual single-atom catalysts for enhanced COOH* spillover and electrocalytic CO_2 reduction activity. *Angew. Chem., Int. Ed.* **2025**, *64*, e202504423.
[130] Wang, S. Y.; Jiang, J. C.; Wang, D. S.; Wang, K. Unlocking the free radical evolution for directed conversion of furoic acid to 2,5-furandicarboxylic acid over lattice-distorted MnO_x. *Angew. Chem., Int. Ed.* **2025**, *64*, e202515012.
[131] Cheng, X. F.; He, J. H.; Ji, H. Q.; Zhang, H. Y.; Cao, Q.; Sun, W. J.; Yan, C. L.; Lu, J. M. Coordination symmetry breaking of single-atom catalysts for robust and efficient nitrate electroreduction to ammonia. *Adv. Mater.* **2022**, *34*, 2205767.
[132] Liu, G. Q.; Zhang, H.; Wang, P. F.; Gao, C.; Zhuang, Z. C.; Wang, D. S.; Zhan, S. H. Atomic-level design of acid-base pairs in oxides for selective catalytic reduction of nitrogen oxides with ammonia. *Angew. Chem., Int. Ed.* **2025**, *64*, e202509362.
[133] Wu, Z. Y.; Karamad, M.; Yong, X.; Huang, Q. Z.; Cullen, D. A.; Zhu, P.; Xia, C.; Xiao, Q. F.; Shakouri, M.; Chen, F. Y. et al. Electrochemical ammonia synthesis via nitrate reduction on Fe single-atom catalyst. *Nat. Commun.* **2021**, *12*, 2870.
[134] Zhao, J.; Gao, G.; Li, T.; Deng, Y. T.; Wang, B.; Dai, P. H.; Li, H. S.; Zhuang, Z. C.; Yang, J. R.; Wang, J. Z. et al. Single atom-substituted chalcogenides with anion vacancy bonded on graphene nanotubes for achieving "1 + 1 + 1 > 3" synergistic enhanced sodium storage. *Angew. Chem., Int. Ed.* **2025**, *64*, e202512028.
[135] Zhang, J. C.; Yang, H. B.; Liu, B. Coordination engineering of single-atom catalysts for the oxygen reduction reaction: A review. *Adv. Energy Mater.* **2021**, *11*, 2002473.
[136] Ma, R. Z.; Zhang, J.; Gong, J. X.; Lin, Y. X.; Zhang, J. L.; Huang, Z. Q.; Chang, C. R.; Liu, S. J.; Zhu, W.; Wang, Y. X. et al. The cooperative effects of the Rh–M dual-metal atomic pairs in formic acid oxidation. *Angew. Chem., Int. Ed.* **2025**, *64*, e202503095.
[137] Chen, Y. X.; Meng, Z. H.; Wei, X. L.; Wu, M. J.; Xiong, Y. F.; Tang, H. B.; Wang, R.; Tian, T.; Wang, D. S.; Tang, H. L. Tellurium-nitrogen-carbon support boosting platinum catalysis in high-efficiency proton exchange membrane fuel cells. *Angew. Chem., Int. Ed.* **2025**, *64*, e202512315.
[138] Gawande, M. B.; Fornasiero, P.; Zbořil, R. Carbon-based single-atom catalysts for advanced applications. *ACS Catal.* **2020**, *10*, 2231–2259.
[139] Chen, Y. J.; Ji, S. F.; Chen, C.; Peng, Q.; Wang, D. S.; Li, Y. D. Single-atom catalysts: Synthetic strategies and electrochemical applications. *Joule* **2018**, *2*, 1242–1264.
[140] Yang, J. R.; Li, W. H.; Wang, D. S.; Li, Y. D. Electronic metal–support interaction of single-atom catalysts and applications in electrocatalysis. *Adv. Mater.* **2020**, *32*, 2003300.
[141] Lokhande, A. C.; Qattan, I. A.; Lokhande, C. D.; Patole, S. P. Holey graphene: An emerging versatile material. *J. Mater. Chem. A* **2020**, *8*, 918–977.
[142] Qin, L.; Ding, R. M.; Wang, H. X.; Wu, J. H.; Wang, C. H.; Zhang, C. H.; Xu, Y.; Wang, L. C.; Lv, B. L. Facile synthesis of porous nitrogen-doped holey graphene as an efficient metal-free catalyst for the oxygen reduction reaction. *Nano Res.* **2017**, *10*, 305–319.
[143] Chen, C.; Ou, W.; Yam, K. M.; Xi, S. B.; Zhao, X. X.; Chen, S.; Li, J.; Lyu, P.; Ma, L.; Du, Y. H. et al. Zero-valent palladium single-atoms catalysts confined in black phosphorus for efficient semi-hydrogenation. *Adv. Mater.* **2021**, *33*, 2008471.
[144] He, T.; Song, Y. Y.; Chen, Y.; Song, X. W.; Lu, B. Z.; Liu, Q. M.; Liu, H. T.; Zhang, Y.; Ouyang, X. P.; Chen, S. W. Atomically dispersed ruthenium in carbon aerogels as effective catalysts for pH-universal hydrogen evolution reaction. *Chem. Eng. J.* **2022**, *442*, 136337.
[145] Wang, W.; Wu, Y. X.; Lin, Y. X.; Yao, J. X.; Wu, X. S.; Wu, C. Q.; Zuo, X. Q.; Yang, Q.; Ge, B. H.; Yang, L. et al. Confining zero-valent platinum single atoms in α-MoC_{1-x} for pH-universal hydrogen evolution reaction. *Adv. Funct. Mater.* **2022**, *32*, 2108464.